Field Emission from Carbon Nanotubes Deposited on Platinum and Nickel / Nickel Oxide Multilayers

by

Belle Ewei Wang
B. S. Electrical Engineering and Computer Science (1999)
Massachusetts Institute of Technology

Submitted to the Department of Electrical Engineering and Computer Science
in Partial Fulfillment of the Requirements for the Degree of
Master of Engineering in Electrical Engineering and Computer Science

at the
Massachusetts Institute of Technology
May 22, 2000
June 2000

Author_____
Department of Electrical Engineering and Computer Science
May 22, 2000

Certified by_____
Akintunde I. Akinwande
Associate Professor of Electrical Engineering
Thesis Supervisor

Accepted by_____
Arthur C. Smith
Chairman, Department Committee on Graduate Theses

Field Emission from Carbon Nanotubes Deposited on Platinum and Nickel / Nickel Oxide Multilayers

by
Belle Ewei Wang

Submitted to the Department of Electrical Engineering and Computer Science
in Partial Fulfillment of the Requirements for the Degree of
Master of Engineering in Electrical Engineering and Computer Science

May 22, 2000

ABSTRACT

Although carbon nanotubes have been shown to be excellent field emitters, very little is known about the emission mechanism. This work strives to gain insight on field enhancement in films of single-walled carbon nanotubes by studying the internal field emission between the back contact metal and the nanotubes, and the external field emission between the nanotubes and vacuum. Test devices of different work functions were fabricated from platinum and from nickel / nickel oxide. Nickel oxide was deposited by e-beam evaporation or grown by thermal oxidation and characterized by Auger electron spectroscopy, x-ray diffraction and ellipsometry. Carbon nanotubes were deposited onto these test structures and current-voltage measurements were taken. Fowler-Nordheim plots were constructed from this data and analyzed. It was determined that external field emission was most likely to be responsible for electron emission.

Thesis Supervisor: Akintunde I. Akinwande
Title: Associate Professor of Electrical Engineering

Acknowledgements

I would like to give many thanks my thesis supervisor Tayo Akinwande for taking a chance on me and believing in my work. I have learned an incredible amount in just one year of working with him. I am also grateful to the other members of his research group, especially my officemate John Kymissis, for answering all my questions, big and small.

Table of Contents

List of Figures

List of Tables

Chapter 1: INTRODUCTION

1.1 Background and Motivation

Field emitters have been studied extensively for use in vacuum microelectronic devices and flat panel displays. The main challenge in these devices has been that of producing stable, but high current densities at low operating voltages. As of now, high operating voltages are still required, which make integration with solid-state drivers very difficult and the energy efficiency low.

The geometry and material play a large role in determining the properties of the field emission device. Field emitters can take the form of patterned arrays or films; and metals, silicon or carbon-based materials are often used to build emitters. The key attraction for using silicon is that it can be uniform, reliable, and compatible with integrated circuit technology. Unfortunately, it has a high work function; and surface contamination often induces unstable current over long periods of time [1]. The attractions for using carbon-based materials include a wide bandgap, a low electron affinity, and high chemical and mechanical stability [1].

Diamond emitters exhibit high current density and stability, high thermal conductivity, and low field emission behavior [1]. It has also been found that diamond's (111) crystal planes experience very robust negative electron affinity (NEA) at very low electric fields (<1V/μm) [2]. Negative electron affinity materials have a work function such that the vacuum level lies below the conduction band edge. Thus, electrons that are present in the conduction band can therefore readily escape the surface [3]. However, p-type diamond samples are not able to take advantage of the NEA property because the valence band which contains the electrons is ~5eV below the vacuum energy level. Electrons must be emitted into vacuum via Fowler-Nordheim emission [2]. It would be more advantageous to use n-type diamond, but effective and reliable n-type dopants have not been found yet. Common silicon n-type dopants (such as nitrogen, phosphorus, and arsenic) either occupy an energy level in diamond lower than vacuum or have very low solubilities in diamond [4]. The I-V characteristics of undoped diamond films were found to be significantly influenced by its non-diamond carbon contents [1]. Based on the central idea that diamond has negative electron affinity, several studies of electron emission from diamond have postulated that electron emission from diamond can be

controlled by the contact metal / diamond Schottky barrier [2, 5]. A competing theory is that electron emission is controlled by the diamond / vacuum barrier [6]. Gröning et al believe that diamond has a high work function, contrary to some reports in the literature. However, they showed that a high surface field enhances current from diamond surfaces even though the average applied field is very low [6]. They demonstrated that the devices have high surface fields by making energy distribution measurements [6, 7]. It is postulated that the high surface field (and hence field enhancement) is due to surface asperities with small radii.

Carbon nanotubes have small radii and high aspect ratio. The small tube radii make carbon nanotubes ideal candidates for field emission. They exhibit high current densities at low operating voltages [8], stable electron emission, and adequate luminance (in displays) [9]. Their physical shape is also favorable for producing high surface electric fields, which is critical for field emission. Carbon nanotubes are currently being studied extensively for use in field emission applications.

1.2 Problem Statement

Although carbon nanotubes have been found to be one of the most efficient field emitters, the mechanism in not fully understood. This work will try to gain insight on electron emission from carbon nanotube films by studying the emission current as a function of the metal used as a contact to the carbon nanotube. Our objective is to investigate the role of the back contact metal / carbon nanotube Schottky barrier (internal field emission) versus the carbon nanotube / vacuum interface (Fowler-Nordheim emission) in determining emission current.

1.3 Approach

The two main stages of the work will be fabricating test devices and conducting field emission tests. Test devices were fabricated using two different material combinations: platinum and nickel / nickel oxide. Platinum was chosen because its high work function will have a lower barrier to the carbon nanotubes; while nickel oxide was chosen because it is a p-type, wide bandgap semiconductor, which is expected to have a reduced internal barrier to carbon nanotubes. Most of this effort will involve investigating how to create quality nickel oxide in the laboratory and how to incorporate it into

devices. Field emission testing will entail applying carbon nanotubes to the test devices and conducting current-voltage tests.

1.4 Organization of Thesis

The second chapter will present important background information on field emission, carbon nanotubes, and nickel oxide. The next two chapters will discuss the experiments and the results — chapter 3 covering fabrication of nickel oxide and chapter 4 on carbon nanotube field emission. Concluding remarks and recommendations are made in chapter 5. Supplementary graphs are located in the appendix.

Chapter 2: TECHNICAL BACKGROUND

2.1 Field Emission

In order to extract electrons from a material (usually a metal or a semiconductor), energy must be applied to free the electrons from the surface. The amount of energy required depends upon the material's Fermi level, μ, and the work function, ϕ. The Fermi level is defined as the highest occupied electronic level in the conduction band [10], while the work function is the energy difference between the Fermi level and a field-free vacuum near the surface. It is the surface energy barrier that prevents electrons from leaving the material. Figure 2.1 depicts these energy levels for a metal [11].

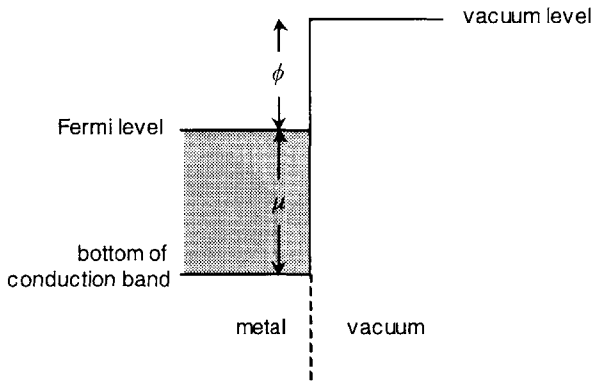

Figure 2.1: Potential Energy Diagram for Electrons in a Metal

There are three commonly used ways to remove electrons from a material. These are thermionic emission, photoemission, and field emission. The first two cases abide by the laws of classical physics in which electrons emitted are given sufficient energy to overcome the surface potential barrier. If the energy of the barrier is greater than that of the incident flux, electrons cannot be emitted. In thermionic emission, the material is heated so that electrons acquire sufficient kinetic energy E_x that is greater than the barrier height: $E_x \geq \phi + \mu$. In photoemission, the material is irradiated with light having energies greater than the work function such that electrons at the Fermi level acquire enough energy to surmount the surface barrier: $h\nu \geq \phi$ [11].

Field emission, on the other hand, does not require electrons to acquire sufficient energy to surmount the surface barrier. Rather, electrons are transmitted through the barrier. An applied electric field deforms the barrier such that unexcited electrons can leak through it. This phenomenon is called tunneling; and it is based on the quantum-

mechanical principle that small particles like electrons exhibit wavelike behavior. Thus, for electrons of kinetic energy E_x (x is the emission direction), the application of a field F results in a barrier height of $\phi + \mu - E_x$ and reduces the barrier thickness to $(\phi + \mu - E_x) / Fq$. ($q = 1.6 \times 10^{-19} C$ — the charge of an electron.) If the barrier becomes thin enough, barrier penetration will occur with finite probability [11]. (This is depicted in Figure 2.2.)

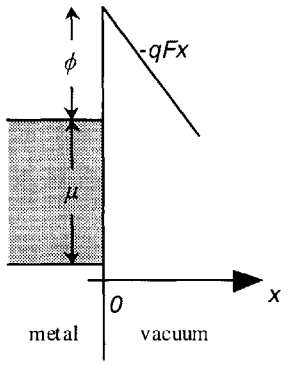

Figure 2.2: Potential Energy Altered by an External Electric Field

The tunneling current density is approximated by multiplying together the transmission probability per electronic state, $D(E_x, F)$, and the product of the occupational probability of the state and the flux of electrons in the x direction, $N(E_x)$ [12]. ($N(E_x)$ is also known as the supply function.)

$$J(F) = q\int_0^\infty D(E_x, F) \cdot N(E_x) dE_x$$

The transmission probability $D(E_x, F)$ (also called the penetration coefficient) can be calculated using the Wentzel-Kramers-Brillouin (WKB) method [11].

$$D(E_x, F) = \exp\left[-\left(\frac{2m}{\hbar^2}\right)^{1/2} \frac{(\phi + \mu - E_x)^{3/2}}{Fq}\right]$$

This gives a good approximation for $D(E_x, F)$ as determined by Fowler and Nordheim, using Schrödinger's equation [11].

$$D(E_x, F) = \frac{4[E_x(\phi + \mu - E_x)]^{1/2}}{(\phi + \mu)} \exp\left[-\frac{4}{3}\left(\frac{2m}{\hbar^2}\right)^{1/2} \frac{(\phi + \mu - E_x)^{3/2}}{Fq}\right]$$

The flux of incident electrons or the supply function, $N(E_x)$, is derived from Fermi-Dirac statistics and the density of states [11].

$$N(E_x)dE_x = \frac{4\pi mkT}{h^3} \cdot \ln\left(1 + e^{(\mu - E_x)/kT}\right) dE_x$$

This matches very well with the Fowler-Nordheim equation for field emission

$$J(F) = \frac{4}{3} \frac{16\pi me(\mu/\phi)^{1/2}}{h^3(\mu+\phi)b^2} \cdot F^2 \exp\left[-b\frac{\phi^{3/2}}{F}\right]$$

with

$$b = -\frac{4}{3e}\left(\frac{2m}{\hbar^2}\right)^{1/2} \alpha$$

$$\alpha = (1-y)^{1/2}$$

$$y = 3.79\times10^{-4}\frac{\sqrt{F}}{\phi}$$

α accounts for the image force potential. J is in A/cm^2, F in V/cm, and all energies in eV [11].

Further work by Spindt transformed the equation to

$$J(F) = \frac{A}{\phi \cdot t^2(y)} \cdot F^2 \cdot \exp\left[-B \cdot \frac{\phi^{3/2}}{F} \cdot v(y)\right]$$

with $A=1.54\times10^{-6}$ and $B=6.87\times10^{7}$. This representation accounts for image charge effects with the functions $t^2(y)$ and $v(y)$.

The total current I is given by

$$I = \int J ds$$

Assuming that current is uniform over the emitting area a,

$$I = J \cdot a$$

Furthermore, the field at the emitting surface can be related to the applied voltage through

$$F = \beta V$$

β is the local field conversion factor at the emitter surface.

This leads to the modified Fowler-Nordheim equation:

$$I = a_{FN} V^2 \exp\left(\frac{-b_{FN}}{V}\right)$$

with

$$a_{FN} = \frac{\alpha A \beta^2}{1.1\phi} \exp\left[\frac{B(1.44\times10^{-7})}{\phi^{1/2}}\right]$$

$$b_{FN} = \frac{0.95B\phi^{3/2}}{\beta}$$

Rearranging the modified Fowler-Nordheim further yields

$$\frac{I}{V^2} = a_{FN} \exp\left(\frac{-b_{FN}}{V}\right)$$

If I/V vs. I/V^2 is plotted on a semi-log graph, we should get a straight line with intercept $ln(a_{FN})$ and slope $-b_{FN}$. (See Figure 2.3.)

$$\ln\left(\frac{I}{V^2}\right) = \ln(a_{FN}) - \frac{b_{FN}}{V}$$

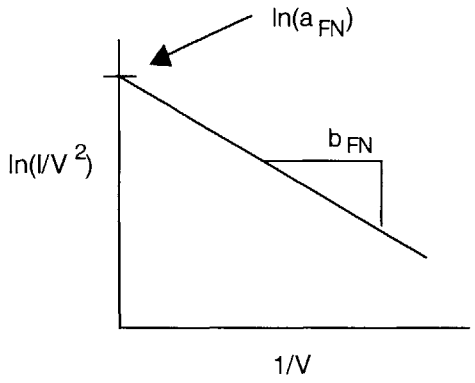

Figure 2.3: A Fowler-Nordheim Plot

A good field emitter has high current densities at low applied voltages. A necessary condition for high emission is a very narrow barrier width or very low barrier height. Since most materials have work functions between 4 and 5eV, it is often easier to narrow the barrier width in order to obtain high current densities. The most common way to narrow the barrier width is the application of a high surface field. High surface fields can be obtained with relatively low voltages if the surface has a small radius (high curvature).

For a carbon nanotube, a prototypical model (Figure 2.4) with be the rounded whisker which can be modeled as a small sphere with radius r located a distance h from a ground plane.

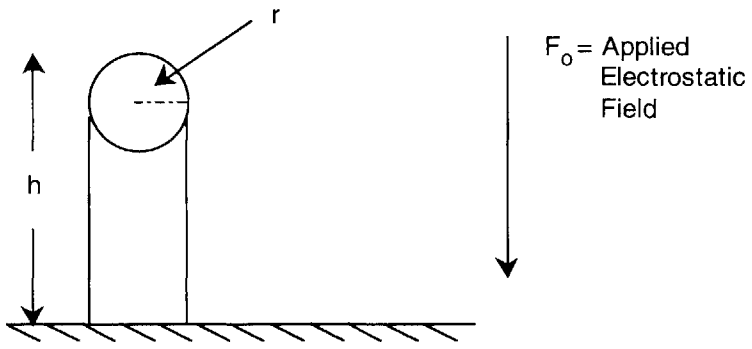

Figure 2.4: Model of a Carbon Nanotube

If θ is the polar angle with the surface normal, then

$$F(\theta) = \frac{h}{r} F_o + 3F_o \cos\theta$$

At the apex,

$$F_{max} = \left(\frac{h}{r} + 3\right) F_o \cong \frac{h}{r} F_o \qquad \text{for } h >> r$$

2.2 Carbon Nanotubes

In 1991, Sumio Iijima discovered carbon nanotubes in the soot of a carbon arc process while trying to create C_{60} molecules. Also referred to as tubular fullerenes, their novel properties have inspired much research in the short time since then.

Structure

Carbon nanotubes can be described as graphene sheets that have been rolled up to form hollow cylinders. They can be classified by the number of graphene layers present – structures with one layer are called single-walled nanotubes (SWNT) and structures with more than one layer are called multi-walled nanotubes (MWNT). Nanotube diameter and length are highly variable. Single-walled nanotubes tend to be 1.0 to 1.4 nm in diameter and on the order of 100 μm in length, while multi-walled nanotube diameters range from 10 to 50 nm and are usually longer than 10 μm [13]. Individual single-walled nanotubes tend to group together in structures called ropes. The number of graphene layers in a MWNT can span from 10 to 20 [8] and are held together by van der Waals forces (and thus separated by the van der Waals distance of ≈0.34 nm) [14]. This distance corresponds to the spacing between typical graphite layers [15]. These long and

wiry structures demonstrate a very high aspect ratio (length/diameter). If we consider only the cylindrical body (and not the tips) of the nanotubes, we can consider them as one-dimensional nanostructures [16].

The graphene sheet is composed of 6-membered carbon hexagon-rings. They can be twisted and rolled different ways to form the cylindrical body. A chiral vector is used to describe the orientation of the carbon rings with respect to the nanotube axis:

$$\boldsymbol{C} = n\boldsymbol{a} + m\boldsymbol{b} = (n, m)$$

$\boldsymbol{a}$ and $\boldsymbol{b}$ are unit vectors in the 2-dimensional plane of the graphene sheet, and n and m are integers. $\boldsymbol{C}$ is perpendicular to the tube axis and follows the circumference of the tube. For example, the vectors $\boldsymbol{a}$ and $\boldsymbol{b}$ are as defined in the following diagram. If the vector $\boldsymbol{OA}$=(6,2) is the chiral vector, then the endpoints of $\boldsymbol{OA}$ will coincide on the tube body.

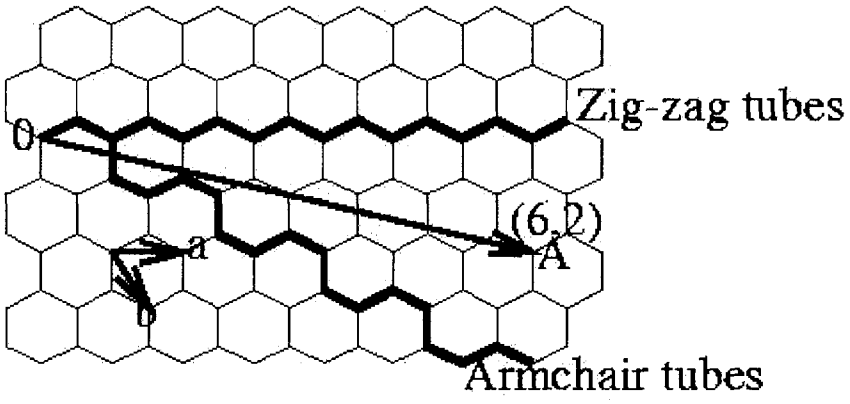

Figure 2.5: Definition of chiral vector

Figure 2.5 [17] also depicts two special kinds of nanotubes – zigzag and armchair. Zigzag tubes have chiral vectors of the form (n, 0), while those of armchair tubes are of the form (n, n). The heavy lines in the diagram indicate what the edges of the respective uncapped nanotubes would look like. Nanotubes with any other kind of chiral vector are considered to have chiral structure. We will see later that the chiral vector helps categorize the electronic structure of the nanotube, which will be described in the *Electronic Properties* section.

The translation vector, T, is defined to be the unit vector of a 1-dimensional carbon nanotube. It is parallel to the nanotube axis and normal to the chiral vector. Using vectors $\boldsymbol{a}$ and $\boldsymbol{b}$, $\boldsymbol{T}$ can be defined as

$$\boldsymbol{T} = t_1\boldsymbol{a} + t_2\boldsymbol{b} \equiv (t_1, t_2)$$

We can use the fact that $\boldsymbol{C}$ and $\boldsymbol{T}$ are normal to each other, to calculate $\boldsymbol{T}$.

$$\boldsymbol{C} \cdot \boldsymbol{T} = 0$$

$$t_1 = \frac{2m+n}{d_R}$$

$$t_2 = -\frac{2n+m}{d_R}$$

d_R is the greatest common divisor of (2m+n) and (2n+m) [16].

The C-C bond length of carbon nanotubes (1.44Å) is known to be slightly larger than that of graphite (1.42Å). The lattice constant for carbon nanotubes is thus

$$a = 1.44\,\text{Å} \times \sqrt{3} = 2.49\,\text{Å}$$

The diameter of the nanotube can be calculated with a, n, and m:

$$d_t = \frac{L}{\pi}$$

$$L = |C| = \sqrt{C \cdot C} = a\sqrt{n^2 + m^2 + nm}$$

where L is the circumferential length of the nanotube.

The introduction of pentagonal rings in the hexagonal configuration leads to curvature at the tips. Even though little is known about the structure of nanotube tips, their small radii of curvature lend well to field emission applications. It is believed that this curvature gives the nanotube tips different electrical properties than the nanotube body. Two reasons for this are (1) the pentagonal rings disturb the pure hexagonal topology of the graphene sheets and (2) the hybridization that occurs between in-plane states and graphitic π-band electronic states. Experiments have shown that the tips of multi-walled nanotubes experience higher chemical reactivity due to a local increase of metallicity [18].

Production

Carbon nanotubes must be produced in the laboratory, as it cannot be found in a natural state on Earth or in space [15]. Two methods have emerged as the most efficient for nanotube production – carbon arc synthesis and laser ablation [16].

As previously stated, it was through the carbon arc method (originally intended for C_{60} fullerene production) that led to nanotube discovery. Not surprisingly, the most prevalent method of producing carbon nanotubes is the carbon arc method. This method relies on an electric arc discharge between two closely spaced (<1mm) graphite electrodes. A current of about 100A is able to pass through and create a plasma between them. Plasma temperatures reach 4000K on average, causing the positive carbon electrode to sublimate and deposit a product on the cathode [15].

The compositions of the electrodes determine the product of the arc discharge. Evaporation of pure graphite rods yield two kinds of products in the reactor – a deposit on the cathode and soot on the reactor walls. Multi-walled nanotubes can be found (along with other nanoparticles) in the deposits, but not in the soot. Co-evaporation of graphite and a catalyst metal produces cathodic deposits, a collaret, web-like structures, and soot in the chamber. The cathodic deposits contain the same materials as mentioned above, with the addition of metallic particles. In the collaret, which encircles the deposit, a high density of single-walled nanotubes can be found, along with amorphous carbon, metallic particles, and graphite products. The same materials can be found in the web-like structures and the soot, except the density of single-walled nanotubes is significantly lower. Co-evaporation with metal is the only way to produce single-walled nanotubes. The metal / carbon mixture plays a large role in determining the quality and quantity of nanotubes [15]. It has been discovered that evaporation with two different bi-metallic catalysts (Fe-Ni and Co-Ni) produce much more single-walled nanotubes than does evaporation with a single catalyst [14].

Another popular method for nanotube production is laser ablation of carbon. A graphite target is heated to around 1200°C in a quartz tube. With an inert gas (such as helium or argon) flowing, the target is vaporized by laser irradiation. The application of two laser pulses was found to minimize the carbon product found in the soot. Carbon product can be found on the graphite target, the quartz tube walls, and downstream from

the flowing gas. Similar to the arc discharge method, evaporation with a pure graphite target yielded only multi-walled nanotubes, while the addition of a transition metal allowed single-walled nanotubes to form. The yield was noticed to improve with an increase in temperature, but drastically decrease with the addition of a metal. Different catalysts produce drastically different yields. When the yields are lower, formation of individual nanotubes becomes favored over the formation of bundles of nanotubes [15].

Other methods for nanotube production include the use of solar energy for carbon vaporization, catalytic decomposition of hydrocarbons, electrolysis, synthesis from bulk polymer, and low-temperature solid pyrolysis [15]. These methods have not provided as much success as the previous two. Also, arrays of nanotubes can be grown (through chemical vapor deposition – CVD), although it is considerably more difficult.

Purification

The as-prepared products from the above methods contain materials other than nanotubes. For example, of the 2-3g of raw material that an optimized single-walled nanotube arc discharge process can produce in a day, only 70% is actually nanotubes [19]. Further processing is required to remove the amorphous carbon, carbon nanoparticles, and catalysts in the samples. These impurities make characterization of nanotubes very difficult. Several separation techniques have been investigated, but success has been limited in this area. No single technique has been able to fulfill all the requirements for nanotubes applications.

Oxidation of the raw material can occur in the gas or liquid phase. In gas phase oxidation, the sample is exposed to air or pure oxygen at high temperatures. In the liquid phase, solutions of water and a strong oxidizing agent, such as HNO_3, $KMnO_4$, or OsO_4, are used to treat the sample [19]. The aim is to decompose any nanoparticles or amorphous carbon [16]. While this method is inexpensive and easily scalable for large quantities, oxidation tends to attack more than impurities. Oxidation occurs preferentially at the tube tips (due to the presence of pentagons and defects) and often leads to openings of the tubes. The tube body is not immune to attack. While multi-walled nanotubes can survive the oxidation treatment (because of their size), many single-walled nanotubes are destroyed in the process. For both types of nanotubes, the

remaining material may also be slightly chemically altered, although the effect is more profound in single-walled ones [19].

Even though nanotubes are insoluble in solvents, liquid phase methods can be applied. Nanotubes that are dispersed in an aqueous surfactant solution can be purified by centrifugation. Yields for multi-walled nanotubes are better than single-walled – multi-walled nanotube content is raised to 90% versus 40% to 70% for single-walled. Pure tubes are often lost in the supernatant, unfortunately. Filtration is possible for single-walled nanotubes, but suffers from pore blocking. The suspension requires constant agitation with an ultrasonic tip to avoid this problem. Downsides to this method are that the tubes are often damaged by the sonication and that samples must already have high concentrations of nanotubes to be effective [19].

Size-exclusion chromatography has been met with success. It is the only purification method that can produce size-selected final products. Throughput is quite low, however [19].

Mechanical Properties

Carbon nanotubes are characterized by high mechanical strength. They are also highly influenced by van der Waals forces. van der Waals forces are observed between individual single-walled nanotubes within a rope and between layers of multi-walled nanotubes. However, van der Waals forces between nanotubes and between nanotubes and a substrate can have a much larger effect by altering the electrical and mechanical properties of the nanotubes.

An example of overlapping nanotubes demonstrates this point. Figure 2.6 shows a molecular mechanics simulation performed by Avouris et al [17].

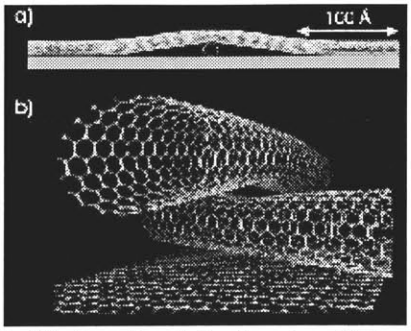

Figure 2.6: Molecular Mechanics Calculations of Overlapping Single-Walled Nanotubes

Figure 2.6 gives different views of axial and radial distortions of overlapping nanotubes. It can be observed that the upper tube is stretched over the lower one, disturbing the symmetry of both. This is due to two opposing forces - the tendency to increase the adhesion energy by increasing the area of contact between the upper tube and the substrate, and the increase in strain energy from the increased tube curvature of the upper tube. The energy of this system can be modeled by

$$E = \int_{tube} (U(c) + V(z(x)))dx$$

where U(c) is the strain energy based on local tube curvature and V(z) is the adhesion energy calculated from the nanotube-substrate interaction potential. Optimization of these two forces determines the shape of the tube profile. Smaller diameter tubes have a higher curvature, and thus withstand distortion from adhesion forces better than tubes with larger diameters. Also, the strain energy increases with the number of layers in multi-walled nanotubes. Hertel et al calculate that for nanotubes of diameter 100Å, the binding energy is 0.8±0.3eV/Å [20]. To put this in perspective, the van der Waals binding energy between individual molecules is only 0.1eV [17]. The high binding energy implies a strong force on the underlying substrate. Thus, for the situation in figure 2.6a, the force at the overlapping tubes can reach as high as 35nN. In addition, the pressure between the nanotubes can reach 10Gpa [20]. These kinds of deformations are what can modify the electrical and mechanical properties of the nanotubes.

That nanotubes conform to the surface morphology of an underlying surface and that nanotubes exert substantial force to those surfaces (whether it be a substrate, a defect in the substrate, or another nanotube) allows for the direct manipulation of individual

nanotubes through atomic force microscopy (AFM). For imaging purposes, the AFM is run in non-contact mode, exerting forces on the order of pN. In order to physically manipulate nanotubes, the AFM must be in contact mode, exerting forces of 10-50 nN [17]. Nanotubes can be bent, straightened, displaced, etc. This is described in detail by Avouris et al and Hertel et al [17, 20].

Electrical Properties

Prediction of the nanotube's electronic structure is based on the 2-dimensional electronic structure of graphite. Thus, the chiral vector is all that is needed to determine whether the structure is either metallic or semiconducting. Armchair tubes (whose chiral vectors satisfy, $n=m$) and tubes where $|n-m|=3i$ (where i is a nonzero integer) are metallic. All others are semiconducting and have an energy gap that is inversely proportional to the tube diameter [21]. Hence, approximately one third of all nanotubes are metallic while the other two thirds are semiconducting.

The energy gap can be determined from the nanotube diameter, d.

$$E_g = \frac{|t| a_{C-C}}{d}$$

$$a_{C-C} = \frac{a}{\sqrt{3}}$$

a_{C-C} is the nearest-neighbor distance on a graphene sheet, a is the lattice constant of the graphene sheet, and $|t|$ is the nearest neighbor tight-binding overlap energy. $|t|$ is 3.13eV for 3-D graphite and 2.5eV for the 2-D case. The value 2.5eV is in good agreement with experimental data [16]. The energy gap ranges from 0 to 1eV [16].

There is much interest in nanotubes because of the one-dimensional nature of conduction [22]. This property makes carbon nanotubes ideal candidates for molecular electronic devices. In order to understand the conductivity of nanotubes, transport theory must be discussed. In macroscopic systems (>1μm), the resistivity and conductivity depend on the material (and not the length of the sample). Classical transport can be used to determine these properties. However, nanotubes are of mesoscopic proportions (~1-100nm), which means that the fullerenes are quite small compared to the characteristic lengths for the motion of electrons. Due to the wavelike interference effects of the

electrons, quantum transport theory must be applied instead [16]. In this case, the length of the sample matters. The relationship between the characteristic lengths determines what transport regime carbon nanotubes operate in.

Three characteristic lengths are important for quantum transport in mesoscopic systems - the mean free path L_m, the Fermi wavelength λ_F, and the phase-relaxation length L_φ. The mean free path is the average length that an electron travels before it is scattered by a scattering center. The Fermi wavelength is the de Broglie wavelength for electrons at the Fermi energy. The phase-relaxation length is the length over which an electron retains its coherence as a wave [16].

In classical transport, momentum and phase relaxation occur frequently ($L_\varphi \ll L_m \ll L$), so the electron is considered a particle. Ohm's Law can be used to determine the resistance and/or conductance. For diffusive motion, many elastic scattering events occur. The phase relaxation length is much longer than the mean free path ($L_m \ll L_\varphi \ll L$), so that the wave function is localized. Resistance becomes very large as L becomes large. Thus, the material acts as an insulator.

Ballistic transport is defined by single-electron conduction with no phase or momentum relaxation ($L \ll L_m, L_\varphi$). The wave function of the electron can be determined by solving Schrödinger's equation. Using the ideal case where there is no electron scattering on a wire of length L connected to two electrodes, the contact resistance can be modeled as

$$R_c = \frac{h}{2e^2} \cdot \frac{1}{M} = R_o \cdot \frac{1}{M}$$

$$R_o = 12.9064 k\Omega$$

where M is the number of energy subbands that fall between the electrode chemical potentials and R_o is the quantized resistance. Contact conductance is merely the inverse of resistance (where G_o is the quantized conductance):

$$G_C = G_o \cdot M$$

$$G_o = 77.4809 \mu S$$

For a metallic nanotube of finite length, M=2 (for the double sublattice degeneracy). Thus, the maximum theoretical conductance for a single-walled nanotube is $G=G_o \cdot 2$ =

154.96μS [23]. This translates to a ballistic transport resistance of about 6kΩ for low bias. However, according to Avouris et al, the measured values turn out to be 38kΩ or higher (in the MΩ range). The resulting non-ohmic I-V curves suggested that the discrepancy in resistance was due to tunneling at the electrode-nanotube barrier. Electron irradiation of the contact regions was found to improve the resistance and the ohmic characteristics [17].

Thess et al measured electrical resistivity of a single rope by the 4-point technique [24]. Resistivity ranged from 0.34×10^{-4} to 1.0×10^{-4} Ω-cm. The wide range of values for resistivity is due to the difficulty in estimating rope diameter. Even discarding all but the most resistive calculation, carbon nanotubes are still the most conductive fibers known. Current-voltage curves were very linear and very stable as well [24].

Another important property is the work function. The work function becomes important when building electronic devices that contain an interface between the nanotubes and a metal or semiconductor [25]. In the past, the value for graphite (ϕ=4.4eV) was often substituted in calculations since no definitive value for carbon nanotubes was available. Ago et al has recently published experimental results in this area. They calculated that the work function of oxidized MWNT (ϕ=4.4-5.1eV) was higher than for purified MWNT (ϕ=4.3eV). Although most data was on multi-walled nanotubes, very preliminary work on purified SWNT obtained from Rice University has been done. Ago et al peg the work function at 4.8eV [25].

Field Emission from Carbon Nanotubes

Several characteristics make carbon nanotubes a good candidate for field emission. Electrically, they exhibit high current densities at low operating voltages [8]. Nanotubes have also demonstrated stable electron emission and adequate luminance in a display [9]. Physically, they are cylindrically shaped, have a high aspect ratio, and have a small radius of curvature at the tip. These features produce high surface electric fields, which are critical for field emission. Recalling the example given in the previous section, typical field emission at an applied voltage of 100V must have a tip radius of 10nm to achieve the necessary surface electric field. Nanotubes are able to meet this size

requirement. In addition, nanotubes have high chemical stability and great mechanical strength.

Possible Applications for Carbon Nanotubes

One logical application for carbon nanotubes would be for nanoscale electronic devices, due to their mechanical strength and novel electronic properties. Their shape also makes them suitable as probe tips for such technologies as atomic force microscopy (AFM) and scanning tunneling microscopy (STM). The remarkable field emission properties naturally suggest uses in field emission applications, such as field emission displays (FED).

Observations of Field Emission Behavior

Much work has been done in trying to characterize the field emission behavior of nanotubes. The range of options in material preparation makes this quite difficult. The following is a sampling of experimental work done so far.

Bonard et al looked at the field emission properties of MWNT in films and single tips. Carbon nanotube films are often studied because they are easier to manipulate. What they concluded was that the nanotube tips were responsible for the field emission, since the tube bodies behaved like graphite (semi-metallic). These tips performed much better than typical field emitters for several reasons. First of all, the cylindrical shape capped off by a tip with small radius increased the electrostatic field at the tip, which led to increased field emission. In addition, the operating voltages were lower compared to other emitters. However, there were some unresolved issues. These emitters experienced a degradation in performance over operating time. Emission failure was sudden and catastrophic for MWNT tips, but gradual for MWNT films. Also, this study indicated that the emitted electrons came from the non-metallic tips (most emitters are metallic). The non-metallic nature of the tips may lead to saturation at high applied voltages and/or huge instabilities in certain voltage ranges. Lastly, the uniqueness of each MWNT tip had led to a variation in electronic state densities at the tip [8].

Obraztsov et al attempted to explain how field emission from carbon nanotube films was possible from such low electric fields. Experimentally, the carbon nanotube

films emitted electrons at electric fields four orders of magnitude less than the electric fields required for metal and semiconductor emitters. They claimed that the bends in atomic layers helped decrease the effective height of the energy barrier for electrons escaping from the film surface [26].

deHeer et al studied the electronic properties of carbon nanotube films. Films of nanotubes, aligned either perpendicular to the substrate or mutually parallel on the surface, were produced. A fine conducting grid was placed 30μm from the film and a voltage was applied between the two. The resulting current-voltage characteristics obeyed the Fowler-Nordheim equation. However, the scientists discovered that up to 90% of the emitted current was being intercepted by the grid - so the actual output current far exceeded the measured current. The behavior of carbon nanotube films was compared with that of CVD diamond films (also touted for its field emission properties). The nanotube films also outperformed the diamond films in other areas. The turn-on field, E_{to}, and the threshold field, E_{thr}, were 4V/μm and 6.5V/μm for the nanotubes, compared to 50V/μm and 80V/μm for the diamond films [28].

Uemura et al installed MWNT films to vacuum tubes to study their use in vacuum fluorescent displays (VFD). Using a CRT-lighting-element, they found the current density on the cathode to be 100mA/cm^2 to 1A/cm^2, with the anode current about 60% of this value. The E_{thr} was only 0.8V/μm, but the driving voltage remained high – the lowest it could be brought down to was 200V. A VFD-like flat panel display was built in a similar fashion. Although its performance was similar to other CRT-lighting-elements, its operation still required hundreds of volts [9].

As of late 1999, Choi et al was able to successfully build a 4.5-inch fully sealed flat panel display using a carbon nanotube composite. Their good results made the prospect of a large area full-color flat panel display more feasible [28].

2.3 Nickel Oxide

Nickel oxide films exhibit good crystallinity, transparency with low resistivity, and controllable transmittance for incident visible light [29]. Because of these properties, nickel oxide has become widely used in opto-electronic and electrochromic devices.

However, as a wide bandgap, p-type semiconductor, nickel oxide also makes a good candidate for use in conducting electrodes.

The most obvious method for producing this material is through oxidation. Although the growth of oxide films on metals is well studied, it is not well understood. Even so, a few points can be made about the oxidation of nickel.

Before actual oxidation, an atomic oxygen chemisorbed layer is formed on the surface of the metal. Oxide islands nucleate and eventually coalesce to produce a 3-5 monolayer thick NiO film. This passivating film forms rapidly, even at low temperatures. If the development of a thicker oxide overlayer is desired, the metal must be exposed to more extreme conditions [30].

The pioneering work on low temperature oxidation by Cabrera and Mott has determined that the growth of oxide surface films appears to be limited by the diffusion of charged particles through the growing oxide film. The cation vacancies in the growing nickel oxide lattice means that the mobility of the nickel cations (and not the oxygen anions) dominates the oxidation process [30]. In addition, when diffusion through the oxide is the limiting factor, growth kinetics can be modeled by the parabolic rate law — thickness $\approx$ time$^{1/2}$ [31].

The crystallinity of the metal and the temperature of oxidation also influence the rate of diffusion. Polycrystalline materials have grain boundaries (while single crystal and amorphous materials do not). Impurities tend to concentrate at these grain boundaries, leading to defect regions in the grown oxide. These regions facilitate ion movement and thus speed oxide growth [32]. Mitra et al investigated the oxidation of polycrystalline nickel at different temperatures. They reported that oxides grown at 400°C and 600°C are dominated by grain boundary diffusion, while oxides grown at 800°C experience grain and lattice diffusion mechanisms in competition [33]. Thus, low temperature oxidation occurs more rapidly with a polycrystalline metal.

Nickel oxide is a wide bandgap semiconductor with a bandgap of 4.0eV [29]. It is also p-type, making it an excellent candidate for hole injection into carbon nanotubes. (For p-type electrical contacts, holes are injected from the Fermi level at the valence band edge. In contrast, holes are injected from the conduction band edge in an n-type contact. The n-type material is much more likely to encounter a large energy barrier to this

injection. Thus, p-type hole-injecting contacts can operate at lower voltages and have higher external power efficiency than its n-type counterparts. [34]) Since carbon nanotubes have work functions of about 4.8eV, they will have a very good contact (or a low barrier) [34] to wide bandgap semiconductors such as nickel oxide or high work function metals such as platinum.

We hypothesize that hole injection from carbon nanotubes into nickel oxide will be enhanced by the internal field emission mechanism due to the reduced barrier between the nickel oxide and the carbon nanotubes. However, this will only be noticeable if the nanotube / vacuum surface barrier is not limiting electron emission and if the nanotubes are relatively short (so that there is no recombination in transport through the nanotubes).

Chapter 3: NICKEL OXIDE FORMATION AND DEPOSITION

3.1 Introduction

Nickel oxide has never been deposited in the Microsystems Technology Laboratory (MTL), hence initial efforts concentrated on investigating deposition techniques. With the available equipment, it was determined that the two feasible possibilities were oxidation of nickel and electron-beam (e-beam) evaporation of nickel oxide.

For each case, a procedure to grow or deposit nickel oxide and evaluate its quality was defined. The fabrication procedures differed dramatically between the two methods.

3.2 Oxidation of nickel

To observe the oxide growth, 100Å of titanium and 5000Å of 99.99% pure nickel were evaporated by e-beam onto 1μm of thermally grown SiO_2. Titanium, which served as an adhesion layer, was necessary to insure that the nickel and its oxide could sustain the entire oxidation test. Deposition took place at 1Å/s in the range of 2.2 - 3.5×10^{-6} Torr. A diffusion tube was used for oxidation. Nitrogen gas flowed during wafer insertion and temperature stabilization. When the temperature reached the desired point, nitrogen was then replaced by oxygen. Temperature, flow rate, and exposure time were varied.

Temperature

Temperature was set at 400°C, 600°C, and 800°C. It was observed that oxidation proceeded incredibly quickly at the higher temperatures (600°C, 800°C). Since only a very thin film was ultimately desired, testing was conducted at 400°C only to ensure controlled growth.

Oxygen Flow Rate

The values for the oxygen flow rate were 1slm, 2slm, and 5slm (slm = standard liters per minute). This was not a critical parameter, so only samples exposed to the 5slm oxygen were analyzed. 5slm was chosen to make sure the process was not transport-limited.

Exposure Time

The nickel was oxidized for 15 minutes, 30 minutes, and 70 minutes to track oxide growth.

3.3 Evaporation of Nickel Oxide

An electron-beam evaporator was used to evaporate 99.9% pure nickel oxide pellets. Both a sapphire and a copper crucible were evaluated. The copper one turned out to be the better choice since it was more thermally conductive. The chamber was pumped to 3.0 - 4.0×10^{-6} Torr before deposition. A liftoff planetary was used. Successful deposition parameters are summarized in the following table.

Table 3.1: Nickel Oxide Electron-Beam Deposition Parameters

Rise	Time	1 min
Soak	Time	3 min
	Power	14-15%*
Pre-deposit	Time	30 sec
	Power	14-15%*
Maximum Power		25%
Deposition Rate		2 Å/s
Tooling		45%
Density		6.67 gm/cm^3
Acoustic Impedance		8.93e05 gm/cm^{2}s

*Actual value based on stability of actual deposition.

The e-beam evaporator undergoes three stages before deposition of the target material occurs. During the rise time, the electron beam ramps from 0% power up to the soak power. The soak time allows the target to be heated up and readied for sublimation. Sparks begin to be seen from the target at around 12-14% power. After extended electron beam exposure and a slight increase in power, a few of the pellets begin to glow orange entirely. The pre-deposit time is aimed at removing any last impurities in the sample before deposition onto the actual sample. During deposition, the beam power is varied automatically by the machine as to maintain the deposition rate specified by the user. The beam power could never go above the maximum power parameter as a safety interlock. 2Å/s seemed to be the optimum deposition rate. Any rate higher than this seemed to require too much power and cause the reactions in the chamber to go out of control. If the

power level was observed to be wildly fluctuating, the deposition rate was adjusted to a value where the power level seemed to be stable (±0.5Å/s).

A quartz crystal microbalance inside the chamber monitored the rate of deposition and the thickness of the deposited layer. It required the tooling, density, and acoustic impedance parameters. The tooling is an experimentally determined ratio to compensate for the difference in the microbalance-measured thickness and the actual thickness. To determine the tooling factor, tooling was initially set at 100% and nickel oxide was deposited until the monitor registered 1000Å on the thickness display. Actual thickness measurements ranged from 420Å to 460Å. To compensate for this discrepancy, the tooling was linearly adjusted. Therefore, the tooling factor was set to ~45%. Since the acoustic impedance of nickel oxide was unknown, a standard number was consistently used.

The entire process required constant monitoring. The nickel oxide pellets seemed to outgas when the electron beam power was increased to about 15%. This caused the pressure in the chamber to increase to unacceptable levels, which ultimately led to the electron beam shutting off. To make sure that the target was ready for deposition, the power was alternated between 14% and 15% during soak time. The goal of this was to initiate controlled outgassing of the material before deposition. If outgassing was not initiated during this stage, then the deposition would fail catastrophically. This was because the sudden increase in beam power at the start of the deposition phase would cause significant outgassing that the ion pump couldn't handle. Oscillating the power from 14% to 15% allowed the material to outgas a little, and then let the ion pump work harder to decrease pressure, outgas the material, work the pump, etc. In this way, the ion pump was not overloaded during deposition.

The deposition process seemed to change the dark green nickel oxide pellets to silver-gray / black wherever the electron beam was aimed. It was unclear at what point

the physical appearance changed or if the chemical composition changed. Hence, fresh nickel oxide pellets were supplied for each deposition.

3.4 Materials Analysis of Nickel Oxide

Four samples were prepared and analyzed. A summary of the method of preparation and resulting characteristics is contained in the following table:

Table 3.2: NiO Sample Characteristics

Method of Preparation	Growth Conditions*	Color
Oxidation of nickel for 15 min	434.1°C 5slm O_2	Peach
Oxidation of nickel for 30 min	433.2°C 5slm O_2	Blue
Oxidation of nickel for 70 min	430.2°C 5slm O_2	Beige
E-beam evaporation of nickel oxide	3.2 – 3.6×10^{-6} Torr 1Å/s	Olive green / transparent

*Growth conditions for oxidation include temperature and oxygen flow rate; chamber pressure and deposition rate for e-beam

Analysis of Chemical Stoichiometry - Auger electron spectroscopy

To determine the chemical composition of each sample produced, Auger electron spectroscopy (AES) was conducted. The surface survey determined which elements to scan for in the depth profile. Since the sputter rate for nickel oxide was unknown, the rate for SiO_2 (200Å/min) was used to keep track of the relative depth sputtered. In addition, the samples were continuously rotated during sputtering to prevent inconsistent sputtering rates within the same material. The depth at which either the nickel or oxygen level dipped below 45% was taken to be the relative oxide thickness. The depth of the sputtered crater was measured with a profilometer to estimate the actual depth sputtered. All depth values were then renormalized to approximate actual oxide thicknesses. These numbers were needed by the ellipsometer to determine the actual oxide thickness. These results are presented later in this section. All graphs in this section have already been renormalized to reflect the correct thicknesses.

The Auger electron spectroscopy surface surveys for the four nickel samples are shown below in Figures 3.1-3.4. The major peaks are labeled with the corresponding

elements. From these scans, it can be seen that the only elements present in significant proportions were nickel and oxygen. Carbon was present in very faint amounts in the oxidized samples. It was probably due to the samples being exposed to air between the nickel deposition and oxidation steps.

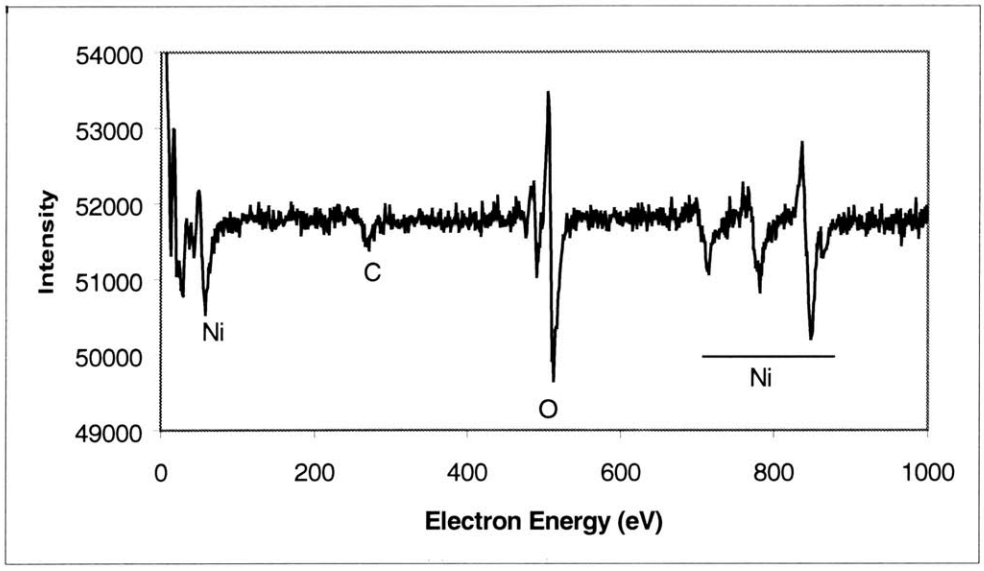

Figure 3.1: Auger Surface Survey – NiO (Ni oxidized at 5slm, 15 min)

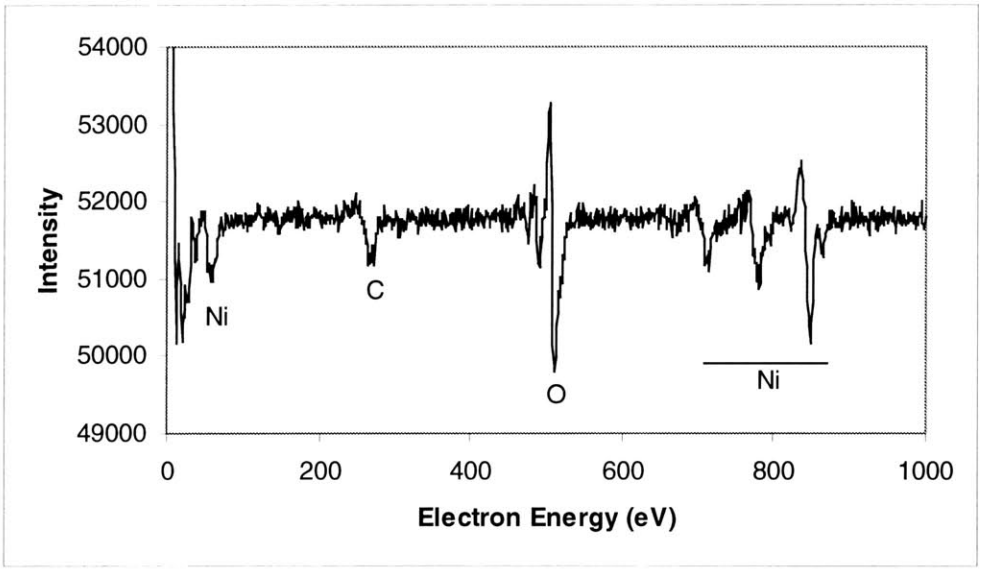

Figure 3.2: Auger Surface Survey – NiO (Ni oxidized at 5slm, 30 min)

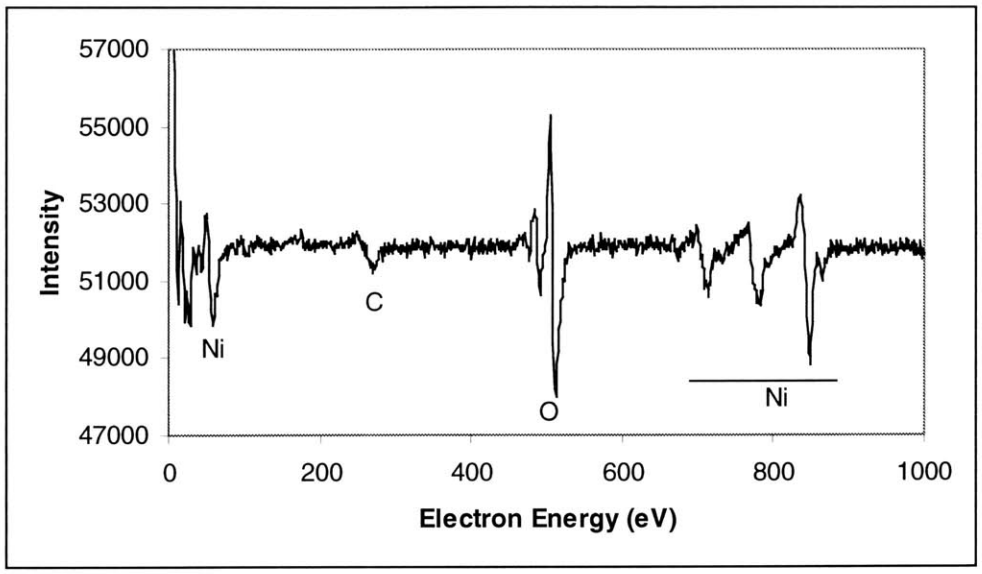

Figure 3.3: Auger Surface Survey – NiO (Ni oxidized at 5 slm, 70 min)

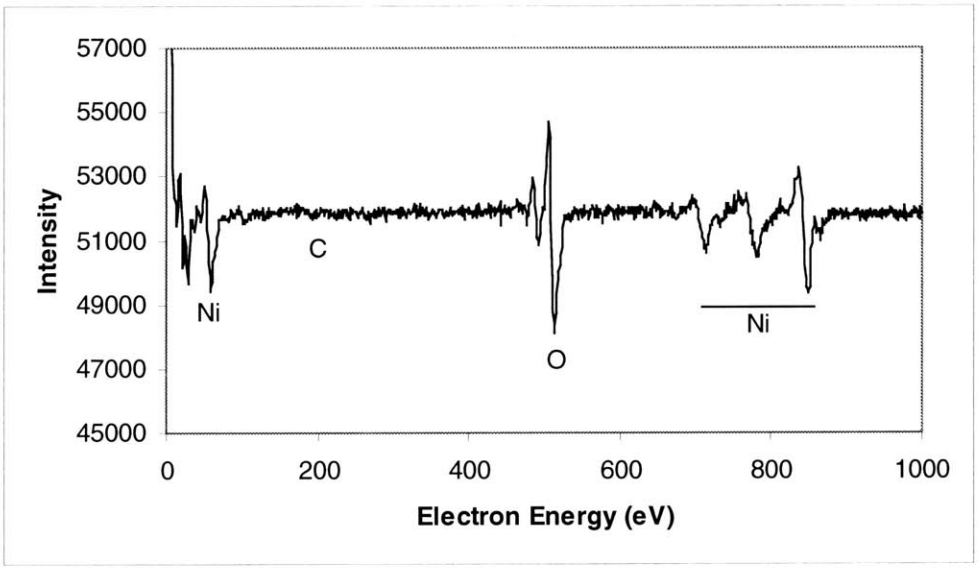

Figure 3.4: Auger Surface Survey – NiO (NiO e-beam evaporated)

Because only nickel and oxygen were present in appreciable amounts, the depth profiles scanned only for those elements. (See Figures 3.5-3.8.) Since the thin layer of e-beamed nickel oxide was deposited directly onto silicon, silicon was scanned for in that one profile. The edge of the oxide layer was determined to be the point where either the

nickel or oxygen level dropped under 45%. For the oxidized samples, this indicated the interface between the thermal oxide and the nickel; and for the e-beam depth sample, the interface between the oxide and the silicon substrate. In all samples, nickel and oxygen was present in fairly even amounts until the next layer was reached. As expected, the longer oxidation times yielded thicker oxides.

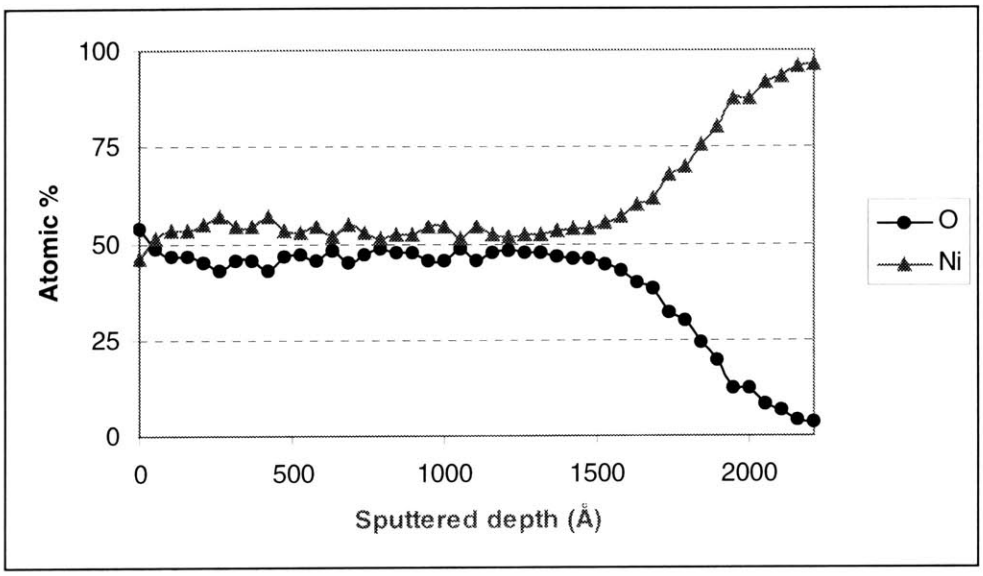

Figure 3.5: Auger Depth Profile – NiO (Ni oxidized at 5slm, 15 min)

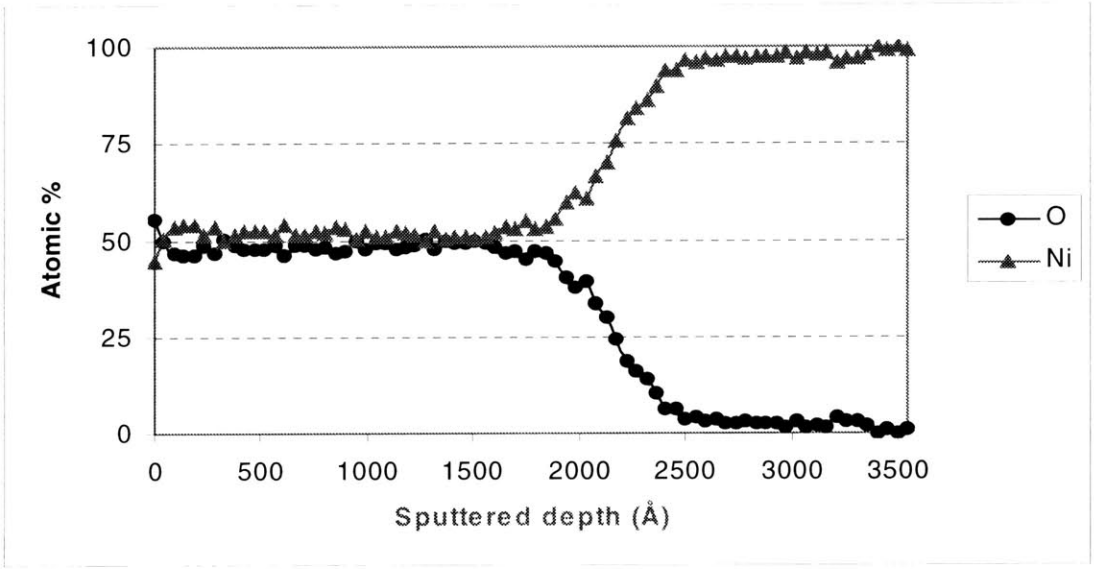

Figure 3.6: Auger Depth Profile – NiO (Ni oxidized at 5slm, 30 min)

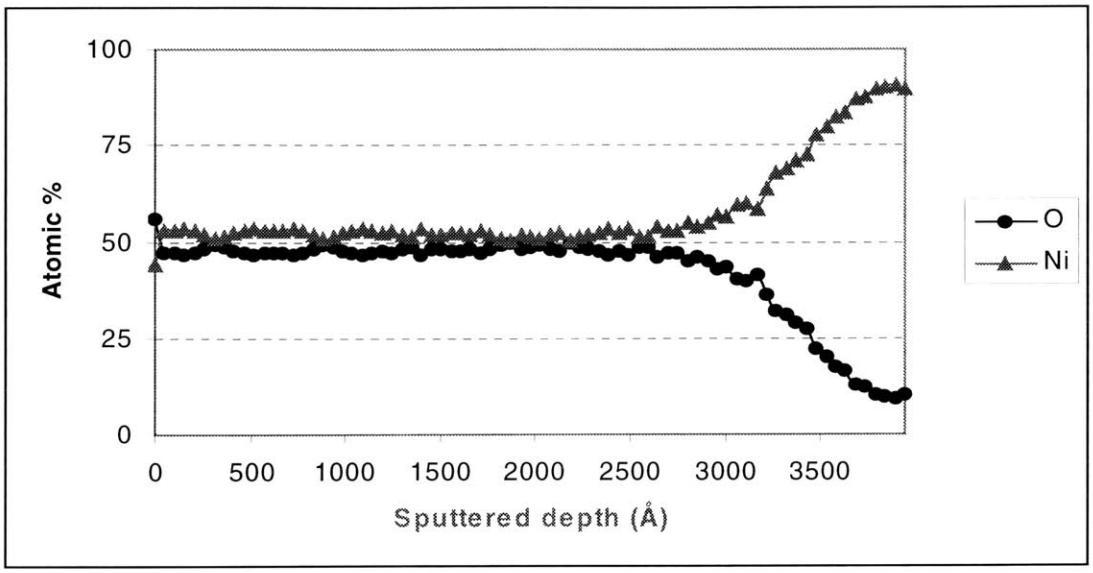

Figure 3.7: Auger Depth Profile – NiO (Ni oxidized at 5slm, 70 min)

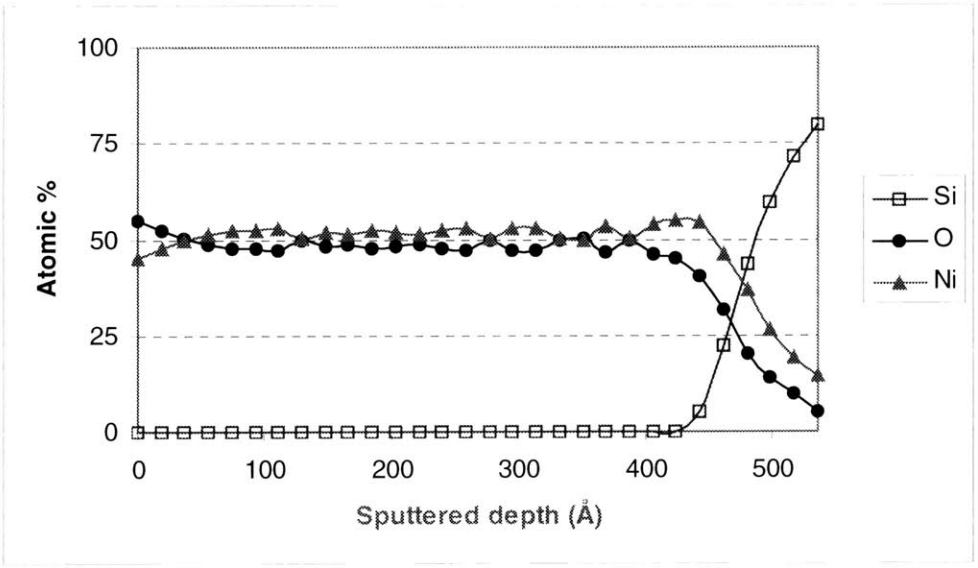

Figure 3.8: Auger Depth Profile – NiO (NiO e-beam evaporated)

Crystallinity Analysis – X-ray Diffraction

The crystallinity was observed with a Rigaku Rotating Anode X-Ray Generator, with 185mm and 250mm Diffractometers. The scans (Figures 3.9-3.12) indicated that the films were polycrystalline with small crystal sizes. Generally, this complicates interpretation of data, since small crystals lead to weaker and broader peaks. Even so, the

most relevant peaks were observed in the scans. The strongest nickel oxide peaks were expected at 2Θ = 37.25° and at 2Θ = 43.29°. Peaks from the silicon substrate were found in the 2Θ=60°-75° range. Slight amounts of tungsten were detected, but this was due to the tungsten filament of the X-ray Generator.

In each of the scans, peaks were found in the nickel oxide range. As expected, for the oxidized samples, the relative intensities of the peaks increase with thicker oxides.

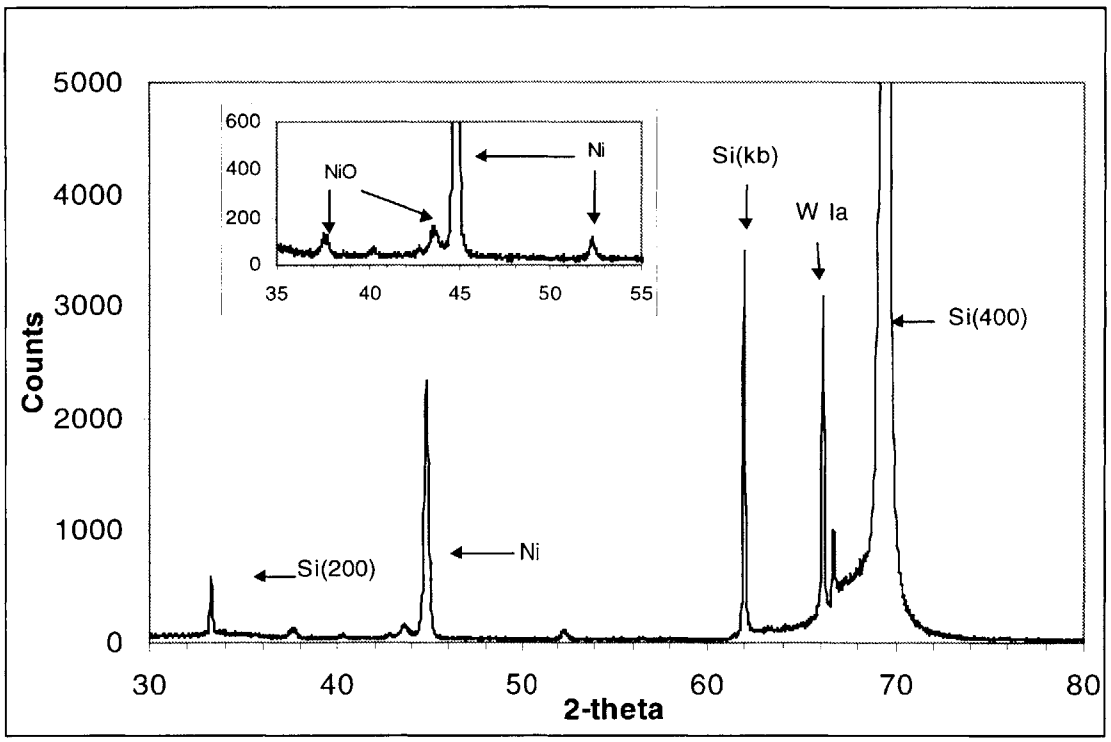

Figure 3.9: X-Ray Diffraction – NiO (Ni oxidized at 5slm, 15 min)

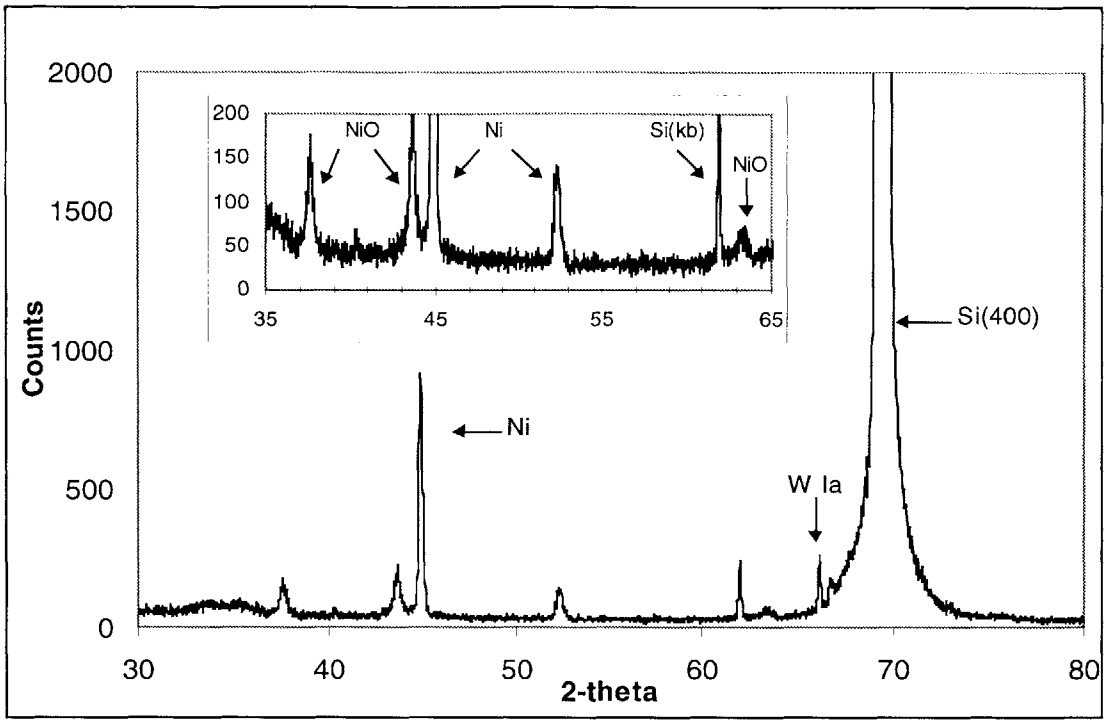

Figure 3.10: X-Ray Diffraction – NiO (Ni oxidized at 5slm, 30 min)

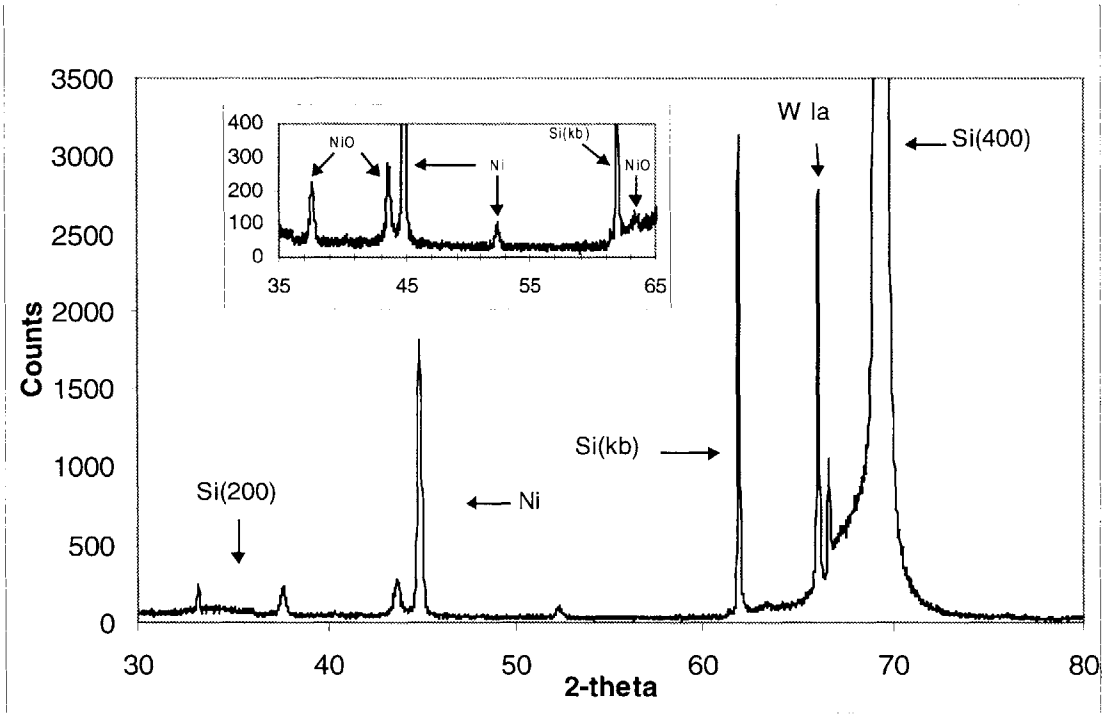

Figure 3.11: X-Ray Diffraction – NiO (Ni oxidized at 5slm, 70 min)

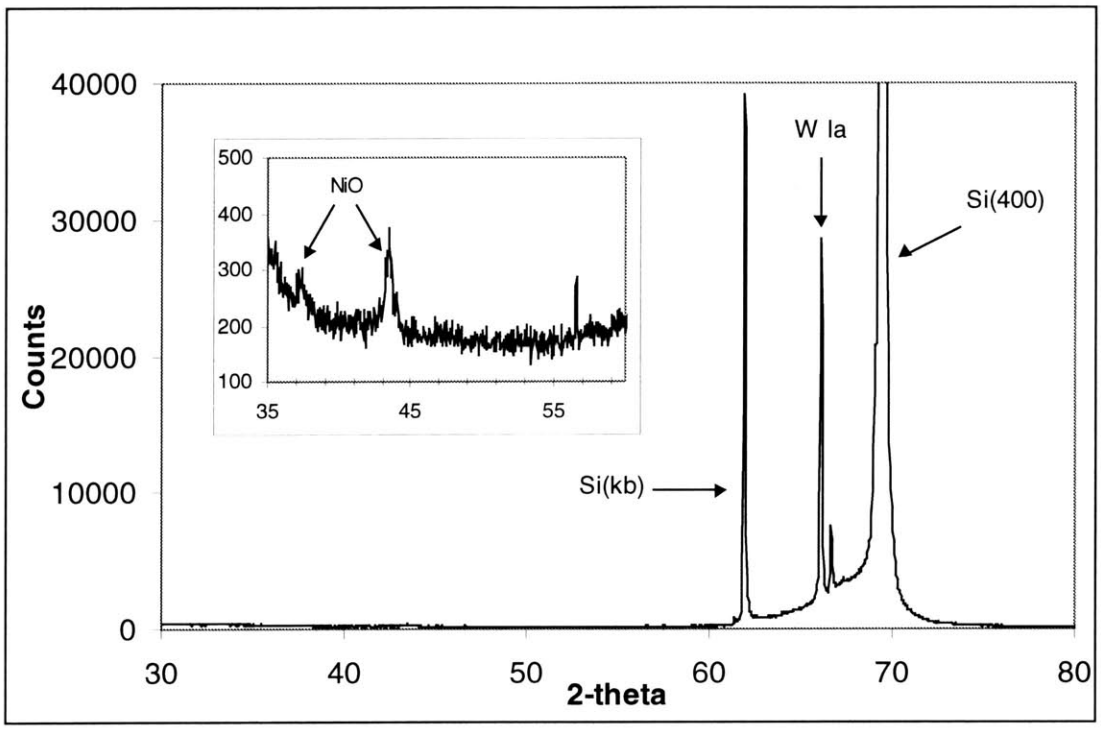

Figure 3.12: X-Ray Diffraction – NiO (NiO e-beam evaporated)

Thickness – Profilometry and Ellipsometry

To get rough approximations for the oxide thicknesses, the actual depths of the sputtered craters (which were measured by the profilometer) were compared to the depths of the craters as measured by the Auger analyzer. (Table 3.3) There is a discrepancy in the measurements for the sputtered depths for the 30-minute and the 70-minute oxidations. It is unclear why the depth for the 70-minute oxidation was smaller than the depth for the 30-minute oxidation, but the data was still analyzable. The ratios (Table 3.3) between these two numbers were applied to the Auger measurement to estimate the oxide interface. (Table 3.4)

Table 3.3: Measured Sputter Depths

NiO Sample Preparation	Sputtered Depth (Å) (from profilometer)	Sputtered Depth (Å) (from Auger)	$\frac{(\text{Sputtered Depth})_{\text{Profilometer}}}{(\text{Sputtered Depth})_{\text{Auger}}}$
15 minute oxidation	2000	4200	0.476
30 minute oxidation	3500	7500	0.467
70 minute oxidation	3100	7600	0.408
E-beam evaporation	400	966.67	0.414

Table 3.4: Estimated Oxide Thicknesses

NiO Sample Preparation	Oxide Thickness (Å) (from Auger)	Calculated Oxide Thickness (Å)
15 minute oxidation	2900	1380.4
30 minute oxidation	4000	1868.0
70 minute oxidation	5600	2284.8
Electron-beam evaporation	766.67	317.4

The values in the last column of the previous table were submitted to an ellipsometer as estimates of the oxide thickness. The ellipsometer was able to calculate n, the refractive index, and the thickness of the electron-beamed nickel oxide. (Values in Table 3.5 were calculated with λ=633nm unless noted.) The average refractive index was comparable to the actual value – $n=2.18$ [35].

Table 3.5: Ellipsometer Results for E-beamed Nickel Oxide

Refractive Index (average)	Oxide Thickness (Å) (average)	Period (Å)
2.047	425.0	1737

Measuring the thickness of the oxidized nickel was slightly more difficult. Fixing n_{NiO} =2.18, n_{Ni}=1.97 ± i3.72, ellipsometer measurements for the first two oxidized nickel samples were obtained. (Table 3.6)

Table 3.6: Ellipsometer Results for Oxidized Nickel

Nickel Oxide Preparation	Oxide Thickness (Å) (average)	Period (Å)
15 minute oxidation	1524.7	1608
30 minute oxidation	1888.0	1608

The thickness for the sample oxidized for 70 minutes required measurement with the λ=830nm laser. (See Table 3.7) The λ=633nm laser could not reach a conclusive measurement even when the refractive index was allowed to vary (the period was too small) and when the refractive index was fixed at 2.18 (no number could be calculated).

Table 3.7: Ellipsometer Results for Nickel Oxidized for 70 Minutes

Refractive Index (average)	Oxide Thickness (Å) (average)	Period (Å)
3.219	2908.3	1348

Although the refractive index and thickness are high compared to estimates, this can probably be attributed to the complicated multilayer sample. The ellipsometer requires that the substrate beneath the layer to be measured to be thousands of angstroms thick. After such a long oxidation, it is expected that much of the nickel was consumed – leaving a less-than-ideal thin substrate layer.

The ratio between the oxide thickness measured by the ellipsometer and by Auger is applied to the crater depth seen by Auger. This produces the actual depth values (Table 3.8) (which are used on the Auger depth profile scans).

Table 3.8: Actual Oxide Thicknesses

Sample Preparation	Oxide Thickness (Å) (actual)	$\frac{(NiO)_{actual}}{(NiO)_{Auger}}$	Crater Depth (Å) (actual)
15 minute oxidation	1524.6	0.526	2209.2
30 minute oxidation	1888.0	0.472	3540.0
70 minute oxidation	2908.3	0.519	3944.4
Electron-beam evaporation	425.0	0.554	535.5

3.5 Discussion and Summary

Both methods of growing nickel oxide appeared to produce stoichiometric compounds. While the chemical analysis of the different samples provided similar results, there was a definite discrepancy in physical appearance in the final samples. The oxide formed by oxidation turned out to be colored – from blue, to yellow to pink.

However, the electron-beam evaporated nickel oxide produced a silver film. This leads one to wonder if the substances are actually very different and/or behave different.

Neither method proved to be substantially better than the other, however. There were several interesting issues that arose for each method for oxide growth. While the e-beam approach was straightforward, the source material experienced changes during the deposition process. The originally green oxide pellets became silver / black where the electron beam hit the sample. It was unclear at what point the sample took on the changed appearance or if the composition of the target remained the same. The sample was also prone to outgassing, which if uncontrolled, would halt the deposition process. It is possible that the outgassing could have altered the material too. These questions prevented reuse of the material. The advantage of e-beam deposition is that monitoring the thickness of the nickel oxide layer is much easier.

The oxidation mechanism presented some unknowns. While the general growth law is known to be parabolic, the growth rate is highly dependent on many variables. In this experiment, only temperature, flow rate, and exposure time could be varied. Using the ellipsometer thickness measurements as data points for curve fitting, the oxidation was modeled with a power function: $t_{ox} = at^b$, with $a=439.23$ and $b=0.4426$. ($r^2=0.9968324461$). Interpolation of the data says that 158.5Å of oxide is formed in the first 6 seconds of O_2 exposure. One minute of exposure yields 439.23Å of oxide. This is very fast initial growth of polycrystalline nickel oxide. This presented a discrepancy with published work on the rate of growth. The films grown here became much thicker in a shorter period of time (a few thousand angstroms in one hour compared to only tens of angstroms of over several hours) [30]. This was probably due to the orientation of the films. Other groups were interested in highly crystalline nickel oxide (which experiences much slower growth), while the crystal orientation was not an issue for the test devices.

Chapter 4: Field Emission Characterization of Carbon Nanotubes

4.1 Test Structure Fabrication

The devices used to measure the field emission were designed by Ioannis Kymissis, a member of my research group. The test structures are designed for evaluating electron emission from thin-films. These devices greatly simplify the evaluation of field emission properties of various thin films.

The device has two electrodes – one for the cathode and one for the anode. A potential is applied between the two electrodes with the cathode connected to ground. The material to be evaluated is deposited on the other contact area, with the anode placed directly above it. Voltage is sourced and current is measured from the anode.

Test structures are arranged in groups of four (See Figure 4.1.). One group of four contains devices of the same cathode area size - 100μm^2. Two other groups contain eight devices total, each with a different contact area size - 10μm^2, 20μm^2, 30μm^2, 60μm^2, 100 μm^2, 200μm^2, 300μm^2, and 600μm^2. These three groups are repeatedly patterned over an entire 4-inch wafer.

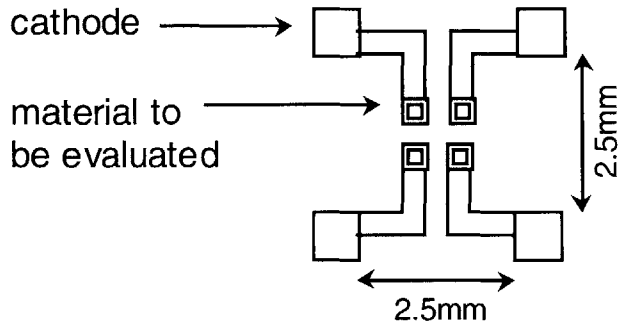

Figure 4.1: A Group of Four Test Structures

Devices were fabricated in the Microsystems Technology Laboratory (MTL) at the Massachusetts Institute of Technology (MIT). The process used to fabricate them is shown in the following table.

Table 4.1: Test Structure Fabrication Recipe

0.	Start with undoped 4-inch silicon wafers
1.	RCA clean (to remove contaminants from the new silicon wafers)
2.	Grow 1μm of thermal silicon dioxide in a diffusion tube
3.	Image reversal lithography (mask#1)
4.	Deposit 100Å of titanium with electron-beam evaporator
5.	Deposit 1000Å of contact material (platinum or nickel / nickel oxide)
6.	Lift-off
7.	SC1 of RCA clean (to remove residual resist / etched metal)
8.	Deposit nitride (by chemical vapor deposition)
9.	Photolithography (mask #2)
10.	Etch nitride (by reactive ion etching)
11.	Remove photoresist (with solvents only)

The thermal silicon dioxide insulates the devices from the silicon substrate. Titanium acts as an adhesion layer for the deposited metals. Two metal stacks were chosen for the test devices – platinum and nickel / nickel oxide. Nitride insulates the test structures from each other and is patterned so as to expose the metal contact areas. Solvents such as acetone, isopropanol, and methanol were used to remove resist. It should be noted that acids or ammonia solutions would attack the nickel oxide.

Three types of devices were fabricated. Although the thickness of the contact material was kept uniform, the actual composition varied. They were:

Table 4.2: Test Devices Used in Field Emission Tests

Contact composition	**Contact color**	**Preparation**
1000Å platinum (Pt)	Silver	e-beam 1000Å Pt
900Å nickel (Ni) / 100Å nickel oxide	Blue	e-beam 960Å Ni oxidize for 1 min at 432.3°C, 5slm O_2
900Å nickel (Ni) / 100Å nickel oxide	Silver	e-beam 900Å Ni e-beam 100Å NiO

4.2 Carbon Nanotube Deposition

Purified carbon nanotubes were obtained from Rice University, where early pioneering work in nanotube research was conducted. Dual pulsed laser vaporization of a metal/carbon target at 1100°C yielded material containing 40-50% single-wall nanotubes. The remaining material consisted of amorphous carbon and residual catalyst particles. To decompose these impurities, the raw material was treated with a 12 hour 2.6 M nitric acid reflux [36]. The process of centrifugation, decanting, rinsing and resuspending with pH 8.0 water was carried out several times to remove any acid. To remove the acid decomposition products, the material was then filtered with a mildly basic solution with pH 11 NaOH and the non-ionic surfactant Triton-X 100. The surfactant impeded the tendency of the nanotubes to clump as solutions were increasingly purified [37]. The nanotubes were then extracted with toluene. Toluene was chosen for ease of filtering and resuspension in other fluids.

Over 90% of their final suspended product ends up being single-walled nanotubes, with the remaining material being graphitized carbon that could not be removed during the nitric acid reflux. There is very little (<1 atomic %) of the metallic precursors, cobalt and nickel (3-15nm in diameter), in the sample. They tend to be carbon-coated, which prevents their removal during nitric acid reflux. In addition, reaction products (polycyclic aromatic molecules with extensive peripheral oxidation) from the nitric acid reflux of the amorphous carbon sometimes form [36]. Sample scanning electron microscope images from Rice University are shown in Figures 4.2-4.3. The first image (Figure 4.2) is what a typical sample should look like:

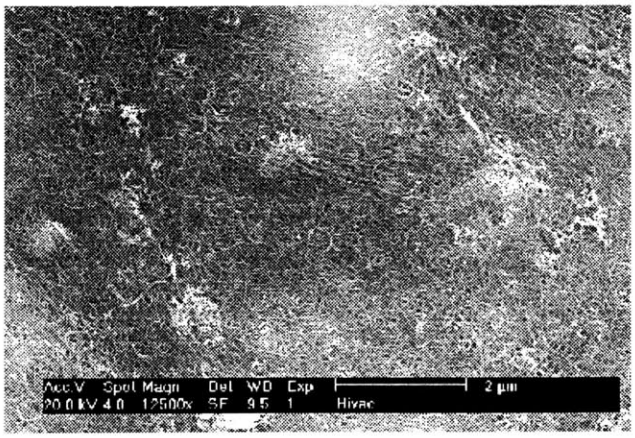

Figure 4.2: A Typical Purified Nanotube Sample from Rice University

The following two SEMs (in Figure 4.3) highlight impurities. The picture on the left contains spherical particles that are metal precursors. The image on the right contains patches of reaction products from the nitric acid reflux.

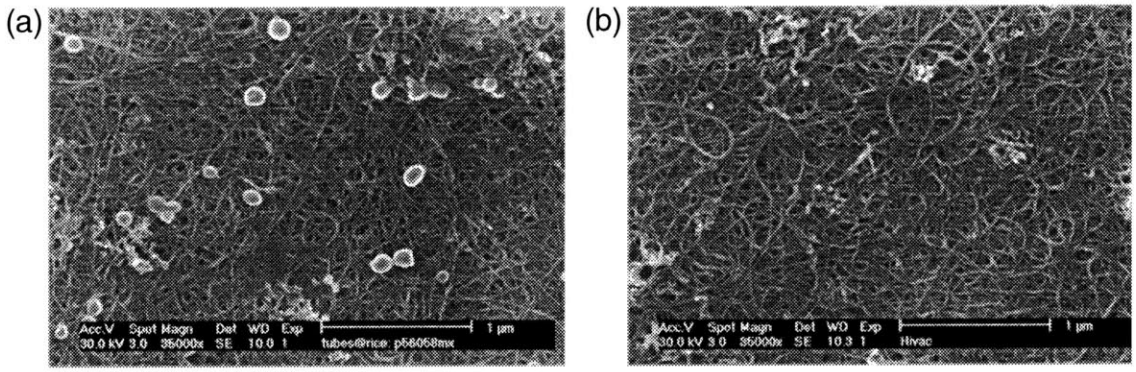

Figure 4.3: Rice Nanotube Samples with (a) Metal Impurities and (b) Nitric Acid Reflux Reaction Products

Rice has characterized their nanotube samples. Their samples contain all single-walled nanotubes that are between 0.2 to 2 µm in length, and approximately 1.2 nm in diameter. The chirality is random. The nanotubes tend to be clustered together in ropes and some tubes may have been opened from the purification process [36].

SEM images of nanotube samples we obtained were taken. They confirmed the high purity of the sample, as no metal catalysts or coatings were found. Thus, further processing was not required. Figure 4.4 shows several intertwined ropes. (The scale bar is 5 µm.) Figure 4.5 was taken on the edge of the mesh of nanotubes. (The scale bar is 1µm.)

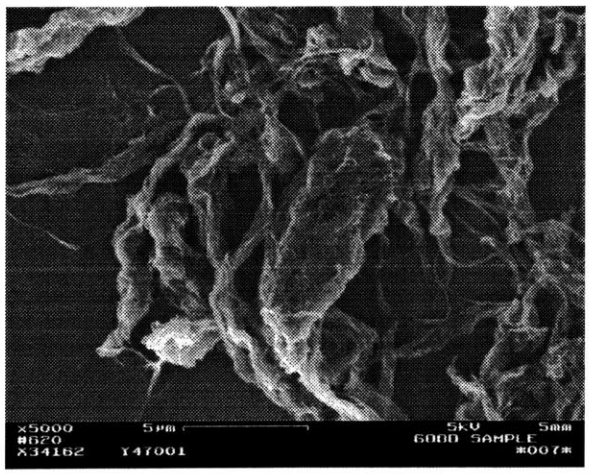

Figure 4.4: Several Intertwined Ropes

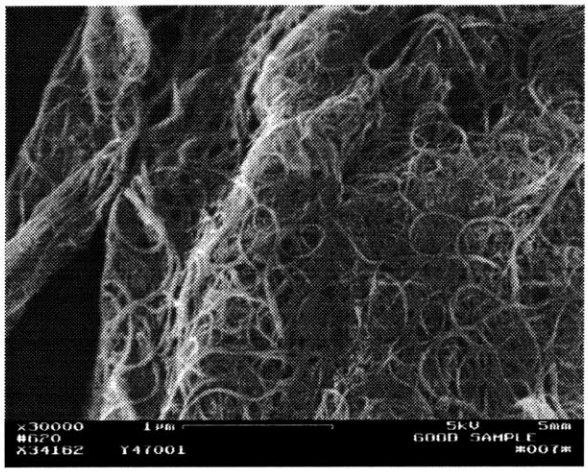

Figure 4.5: Pure Nanotubes

The scale bar for the two SEM images in Figure 4.6 is also 1μm, but the magnification used was much higher. You can see many ropes, but also some strands that look more like individual nanotubes.

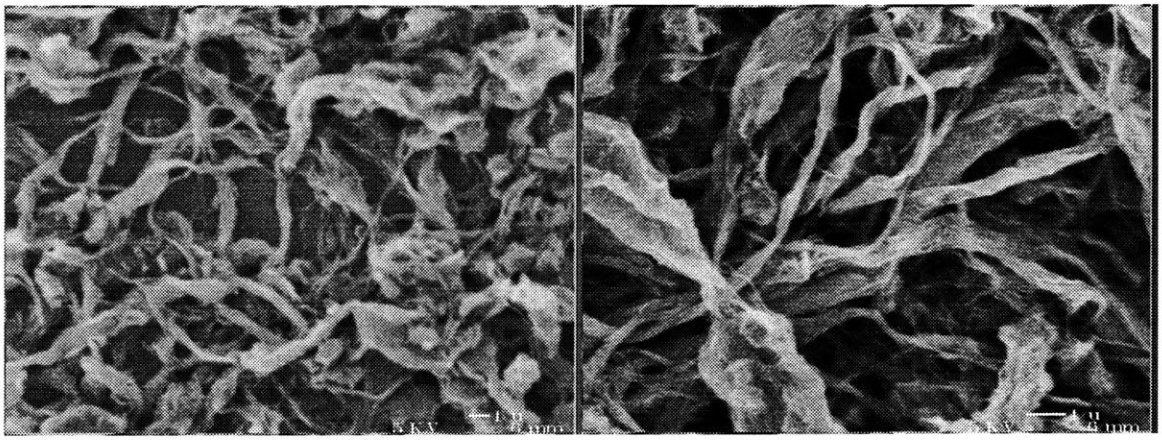

Figure 4.6: Two More SEM Images of the Samples Obtained

In addition, it was possible to observe the approximate density of nanotubes in the solution. Drops of the nanotube solution were micro-pipetted directly onto the test structures. Although drops of nanotube solution applied to the device wafers tended to spread out, it was possible to entirely cover the metal contacts on the test structures. One or two drops of 2.5μL size were sufficient to cover four contact areas. Because of its low vapor pressure, the toluene evaporated quickly. If the nanotubes were not agitated, then they remained on the wafer. Only a few tests (<10) were conducted on each test device, and each site was not reused.

The nanotubes from Rice University were of high purity and needed no further processing. The ability to determine the exact dimensions and orientations of the individual tubes would have been helpful, but these are universal research questions that have not been solved yet. Improvements could be made in application and adhesion of nanotubes to the test device. It was slightly challenging to deposit and retain nanotubes on contact areas that were at most several hundred microns-squared. After deposition, care had to be taken with handling the test substrate, as the fullerenes could be easily rubbed away.

4.3 Field Emission Characterization

Field emission tests were conducted in a probe station under ultra-high vacuum. Pressure in the chamber ranged from 1.5 - 1.9×10^{-9} Torr during testing. For I-V measurements, the cathode was grounded, while voltage was applied to a suspended anode and current measured from the anode. The applied voltage was stepped from 0 to 800V (in 5V increments) at various anode-film spacings. Fowler-Nordheim graphs plotted from this data.

To position the probes, the anode was placed above a contact area that was sufficiently covered in nanotubes, while the cathode was grounded. Anode current was measured while being sourced at 800V. The anode would be lowered towards the wafer until approximately 1μA of current was attained. Then, I-V curves (stepping from 0 to 800V) were taken twice. This entire process was repeated about two more times on the same device. The second iteration positioned the anode so that about 10μA was measured at 800V, while the third iteration placed the anode where 100μA was measured at 800V. A circuit diagram of the entire test system is shown below.

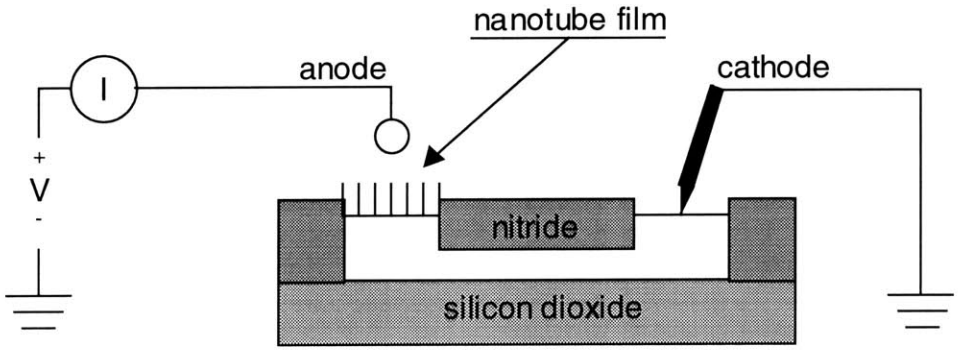

Figure 4.7: Schematic of the Test Circuit

Several I-V measurements were taken on each device. The exact number of plots per device varies, due to the nature of the testing method. Since there was no way to consistently measure anode / film spacing, it was done by moving the probe until a certain current reference point was reached. Because of the exponential increase in current density, a slight decrease in the anode / film spacing would sometimes cause intense sparking. In this situation, it is likely that nanotubes were burned away because removal of the anode exposed an altered test site with noticeably less nanotubes.

Two or three devices of each type yielded satisfactory data. Each run is denoted by a letter and a number. The letter refers to a particular device tested, and the number refers to the run number. A representative plot (from a Ti / Pt device) is shown in Figure 4.8. The I-V plot for each run is in Appendix A.

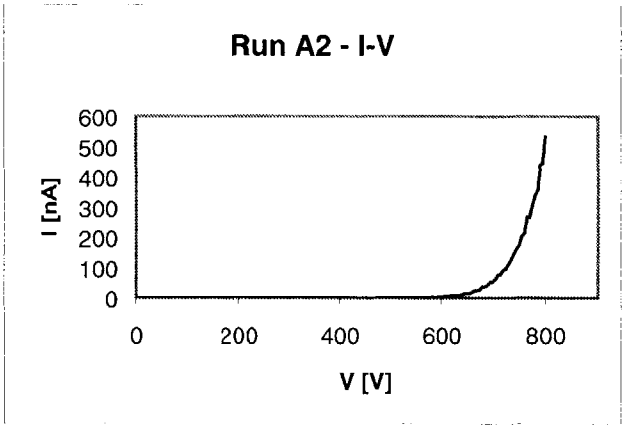

Figure 4.8: An I-V Curve from a Ti / Pt Test Structure

4.4 Analysis of Field Emission from Carbon Nanotubes

To analyze the field emission, we first return to the model of emission from a single nanotube (Figure 2.4). The setup is simplified by modeling the anode and substrate contact area as two parallel plates. The nanotube, of height h and radius r, is most likely perpendicular to the substrate. It is a distance d away from the opposite parallel plate. This simplified setup is shown below.

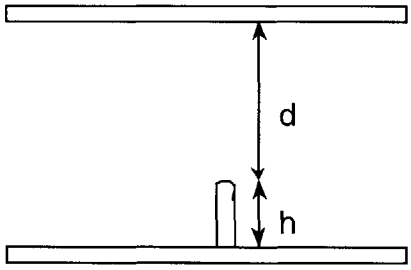

Figure 4.9: A Simplified Setup of Nanotube Field Emission

If there is a potential of V, the average electric field between the plates is

$$F_{avg} = \frac{V}{d}$$

The local field at the tip of the nanotube can be approximated by

$$F_{tip} \cong \frac{h}{r} \cdot F_{avg} = \beta' \cdot F_{avg}$$

$$F_{tip} = \frac{h}{r} \cdot \frac{V}{d} = \beta_{tip} V$$

where β' is the field enhancement factor and β_{tip} is the field factor at the tip. We will assume that this field is uniform over the entire tip radius. To find the current emitted from this single tip, we can plug $\beta=\beta_{tip}$ into the Fowler-Nordheim equation introduced in the *Technical Background* chapter.

$$I_{tip} = a_{FN} V^2 \exp\left(\frac{-b_{FN}}{V}\right)$$

$$a_{FN} = \frac{\alpha A \beta_{tip}^2}{1.1\phi} \exp\left[\frac{B(1.44\times10^{-7})}{\phi^{1/2}}\right]$$

$$b_{FN} = \frac{0.95B\phi^{3/2}}{\beta_{tip}}$$

Hence, the total current for N emitting nanotubes is

$$I = \sum_{i=1}^{N} a_{FN_i} V^2 \exp\left(\frac{-b_{FN_i}}{V}\right)$$

with

$$\beta_i = \frac{h_i}{d \cdot r} = \frac{1}{k_i \cdot r}$$

If we assume a gaussian or poisson distribution of nanotube heights and move the V^2 to the left-hand side, we can simplify the current equation further.

$$\frac{I}{V^2} = a_{FN_{eff}} \exp\left(\frac{-b_{FN_{eff}}}{V}\right)$$

In order to analyze the I-V data from the test devices, the numbers were molded to fit the Fowler-Nordheim equation derived above. To check for the presence of field emission, Fowler-Nordheim plots ($x=1/V$ vs. $y=I/V^2$ on a semi-log graph) were constructed from all the I-V measurements gathered. The plots confirmed that field emission was indeed taking place. The graphs featured relatively straight lines with negative slopes. A

representative plot is shown in Figure 4.10. Fowler-Nordheim plots for all the I-V curves are in Appendix A.

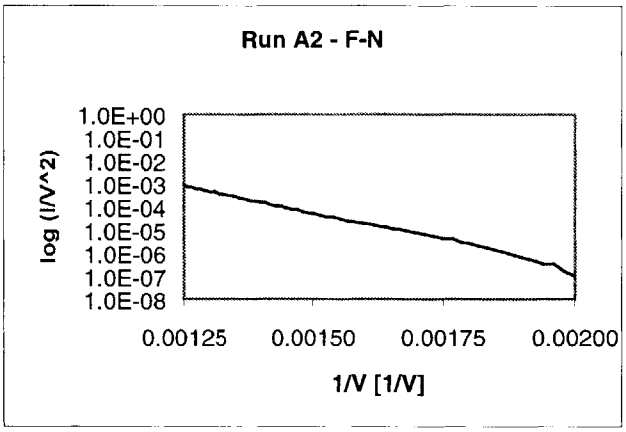

Figure 4.10: A F-N Plot from a Ti / Pt Test Structure

In order to compare the field emission between the different runs, the data was fitted to the function $y=ae^{-bx}$ with $x=1/V$ and $y=I/V^2$. This was done numerically in *TableCurve2D v3*. The r^2 values confirm that the data fit the function well. We can then use the values for b and the work function for carbon nanotubes (ϕ=4.8eV) to calculate β. Values for a, b, and β are listed in Table 4.3:

Table 4.3: Curve-Fitted Values for Fowler-Nordheim

Run	*A*	*B*	r^2	β
Ti / Pt devices				
A1	1066.73	1.1239E+04	0.9967174309	6.1068E+04
A2	859.90	1.1110E+04	0.9976986222	6.1780E+04
A3	16677.49	1.1025E+04	0.9946925481	6.2254E+04
A4	5215.19	1.0106E+04	0.9897788418	6.7914E+04
A5	1032561.70	1.2980E+04	0.9731466117	5.2879E+04
A6	12245517.00	1.4987E+04	0.9908085925	4.5796E+04
B1	200.52	8.6511E+03	0.9498731137	7.9336E+04
B2	2682.89	1.0638E+04	0.9904179316	6.4515E+04
B3	23779.09	1.1505E+04	0.9733047560	5.9655E+04
B4	39086.91	1.1680E+04	0.9875504432	5.8764E+04
C1	4033.99	1.1512E+04	0.9940166045	5.9620E+04
C2	150.92	8.9138E+03	0.9912624190	7.6998E+04
C3	617.56	8.5975E+03	0.9964720429	7.9831E+04
C4	591.63	8.5075E+03	0.9915971034	8.0675E+04

Run	*A*	*B*	r^2	β
Ti / Ni / NiO (ox) devices				
G1	6857.22	1.1516E+04	0.9860836137	5.9601E+04
G2	68.85	7.9536E+03	0.9770602723	8.6294E+04
G3	3275.40	9.6080E+03	0.9963000577	7.1434E+04
G4	279.15	7.6478E+03	0.9773880279	8.9744E+04
G5	877261.59	1.2353E+04	0.9828448153	5.5560E+04
G6	872660.44	1.2381E+04	0.9832671048	5.5436E+04
I1	308.60	9.5295E+03	0.9962131491	7.2023E+04
I2	884.21	1.0321E+04	0.9974150727	6.6497E+04
I3	48.53	6.1402E+03	0.9984932095	1.1178E+05
I4	41.14	5.9805E+03	0.9975209435	1.1476E+05
I5	21.60	4.1782E+03	0.9982212688	1.6427E+05
I6	22.65	4.2527E+03	0.9979459445	1.6139E+05
Ti / Ni / NiO (eb) devices				
K1	101261.67	1.3739E+04	0.9888321317	4.9956E+04
K2	161308.14	1.3896E+04	0.9856761545	4.9392E+04
K3	29284.91	1.1525E+04	0.9967207110	5.9554E+04
K4	11907.05	1.0783E+04	0.9921696056	6.3651E+04
K5	26637.58	1.0112E+04	0.9963113646	6.7871E+04
K6	18680.21	9.8176E+03	0.9963559258	6.9910E+04
N1	29.77	7.6164E+03	0.9983356428	9.0114E+04
N2	7.75	6.5455E+03	0.9861673252	1.0486E+05
N3	5495.35	9.8409E+03	0.9964354985	6.9744E+04
N4	5475.86	9.7975E+03	0.9972315209	7.0053E+04
N5	6660.76	9.2180E+03	0.9960375570	7.4457E+04
N6	5140.20	9.1108E+03	0.9967423175	7.5333E+04
N7	3885.36	1.1323E+04	0.9418229077	6.0615E+04
N8	10958.22	1.3296E+04	0.9962009810	5.1622E+04

Several things can be said regarding β. First of all, the higher β is, the better field enhancement we get. Secondly, β is perhaps the best parameter when comparing field emission amongst different devices. It is independent of emitter area (allowing comparison between *different-sized* devices) and anode distance (so that the spacing between the anode and emitter is irrelevant). β also allows us to make direct correlations between the applied voltage (which is a known quantity) and field emission at the emitter tip, through $F_{tip} = \beta_{tip} V$. Most research done today in field emission uses the electric field as a basis for comparison between devices. However, this electric field is actually the average field, which can be quite different from the field at the emitter tip. It will not

accurately model the barrier deformation due to an applied voltage. Thus, any tunneling current calculations based on this (average) electric field will be incorrect.

There are two areas where emission can occur in this test setup — electron injection into the nanotubes at the device / nanotube interface and electron ejection at the nanotube / vacuum interface. The application of a high electric field in a system such as this will deform the emitter / vacuum interface barrier; and can possibly penetrate into the semiconductor contact to bend its energy bands near the emitter. This produces an accumulation of charge in the well formed near the semiconductor / emitter interface [38]. Electrons can then be injected into the conduction band of the emitter. If the holes can also traverse the length of the nanotube (the emitter), electrons can be easily ejected into vacuum due to the negative electron affinity at the emitter / vacuum interface. This would support quasi-ballistic electron transport within the emitter [5]. A figure diagramming the relative locations of the energy bands is shown in Figure 4.11.

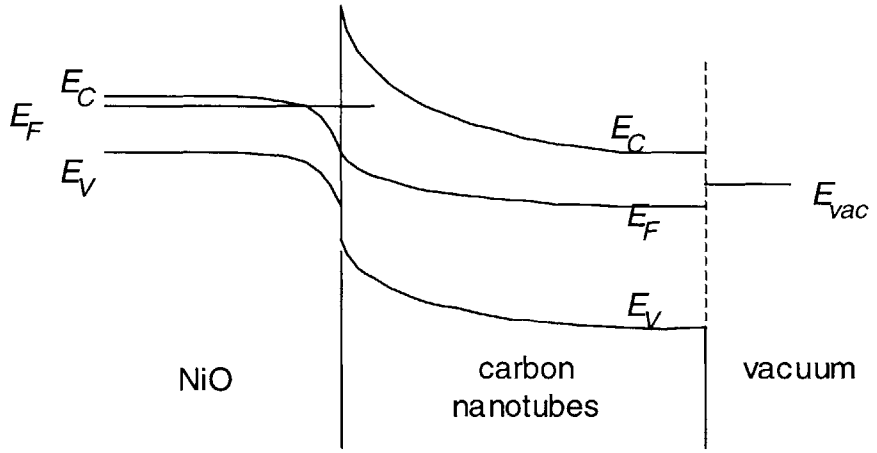

Figure 4.11: Energy Band Diagram

We were hoping to see an improvement in emission by using a high hole-injecting semiconductor like nickel oxide in the test device contact. Although the highest β values are from the nickel oxide device, no real conclusions can be made about the emission efficiency since all the β values are within an order of magnitude of each other. This does not discount the possible utility of nickel oxide contacts, however. Two other factors may have obscured the benefit of nickel oxide in this test setup. First of all, in the attempt to protect the nanotubes from being burned away, voltage was generally kept low. Hence, the applied field could not get high enough to sufficiently penetrate the

device and bend the nickel oxide energy bands. Also, the length of the emitter must be short enough so that carrier recombination cannot occur before electrons reach the emitter / vacuum interface. Although the exact lengths of the nanotubes is unknown, they are almost certainly too long, as they are on the order of microns. Therefore, emission in this experiment is believed to be controlled solely by the barrier deformation at the nanotube / vacuum interface.

Chapter 5: Conclusions and Recommendations

5.1 Conclusions

We conducted a study of the electron emission from carbon nanotubes using a high work function metal (Pt) and a p-type, wide bandgap semiconductor (NiO) as the back contact metal. We studied two approaches to depositing or forming nickel oxide—oxidation of nickel or e-beam evaporation of nickel oxide. Nickel oxide was successfully incorporated into a set of test structures. Auger electron spectroscopy and x-ray diffraction confirmed the quality of the fabricated nickel oxides. The thicknesses of the grown oxides were also quantified.

The field emission tests yielded two main conclusions. First of all, Fowler-Nordheim tunneling was observed, meaning that the carbon nanotubes were successfully field emitting. Second of all, it appeared that the nanotube / vacuum interface (and not the substrate / nanotube interface) was responsible for limiting electron emission at the current levels we studied. Although the field factors for the nickel / nickel oxide devices were better than those for the platinum devices, the difference in β was still small. Thus, altering the contact metal was inconclusive.

5.2 Recommendations

Future work should focus on simplifying the study of each of the field emission mechanisms (internal and external) individually. This would make it easier to predict where subsequent improvements to field emission would be more effective. There are several ways to study this. Materials for the test substrate can be chosen so that the difference between the work functions is more exaggerated. Also, if nanotube samples can be classified so that shorter nanotubes are used, perhaps the internal field emission can be observed more readily.

Besides varying test device materials, different carbon nanotubes samples can be compared – i.e. by studying various purities of nanotubes or by studying single-walled vs. multi-walled nanotubes. Nanotube application could be improved so that cathode coverage is complete and more consistent across test devices. Subsequent field emission testing should address the problem of nanotubes vaporizing at higher applied voltages. In

addition, exploring different anode probe/nanotube configurations could provide other ways to model the field emission.

Appendix A: Current-Voltage (I-V) and Fowler-Nordheim (F-N) Plots

Ti / Pt devices

Run A ($20\mu m^2$ contact area)

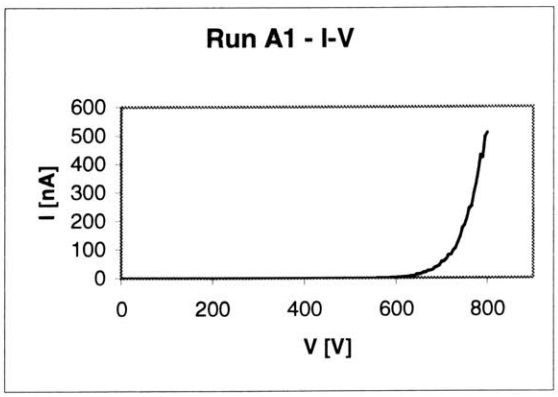

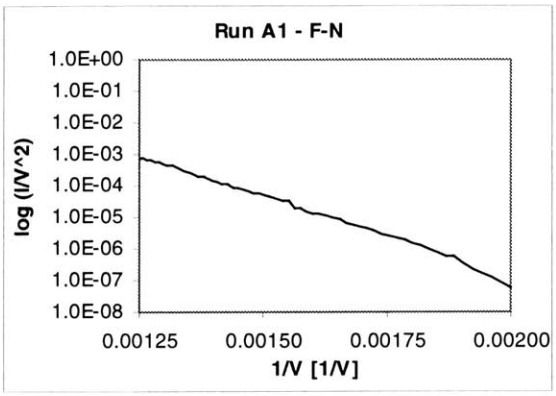

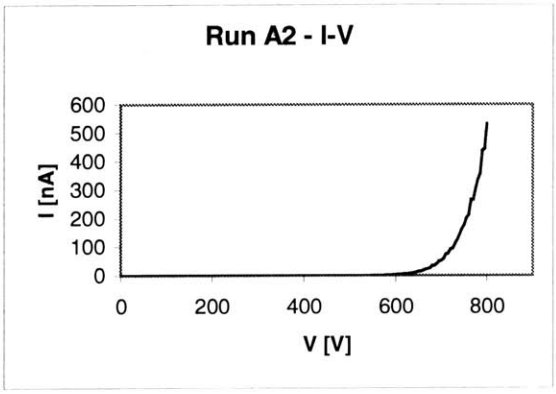

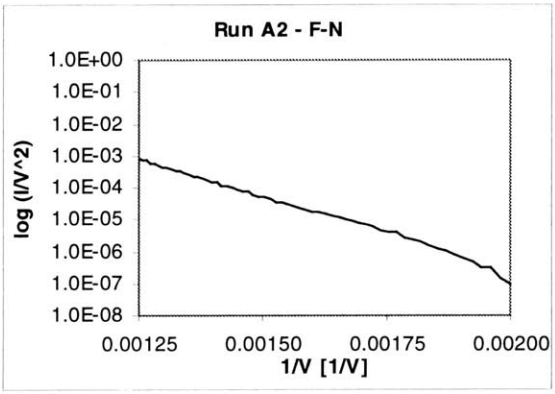

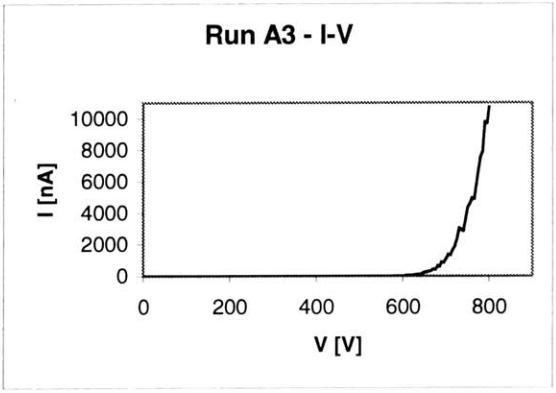

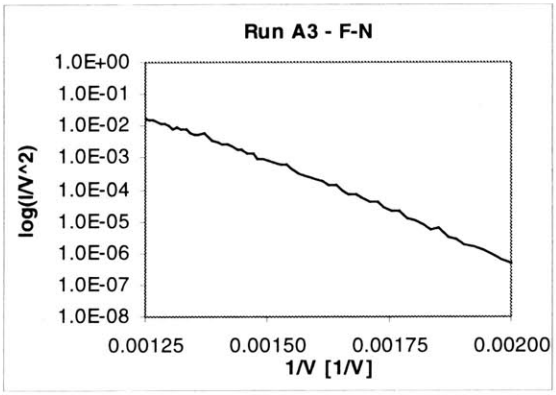

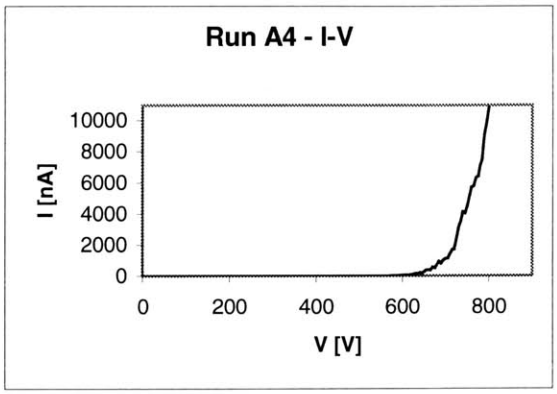
Run A4 - I-V
I [nA]
10000
8000
6000
4000
2000
0
0
200
400
600
800
V [V]

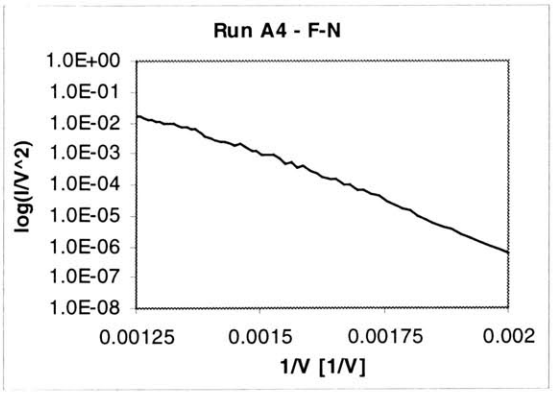
Run A4 - F-N
log(I/V^2)
1.0E+00
1.0E-01
1.0E-02
1.0E-03
1.0E-04
1.0E-05
1.0E-06
1.0E-07
1.0E-08
0.00125
0.0015
0.00175
0.002
1/V [1/V]

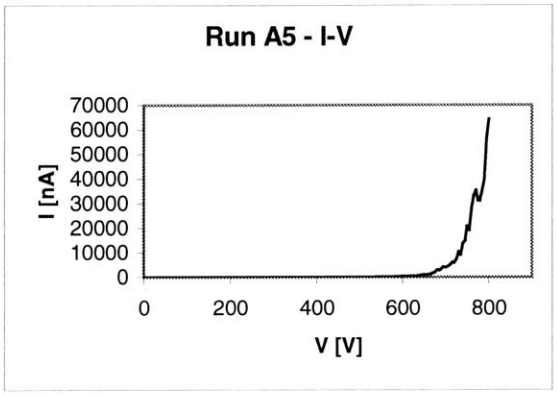
Run A5 - I-V
I [nA]
70000
60000
50000
40000
30000
20000
10000
0
0
200
400
600
800
V [V]

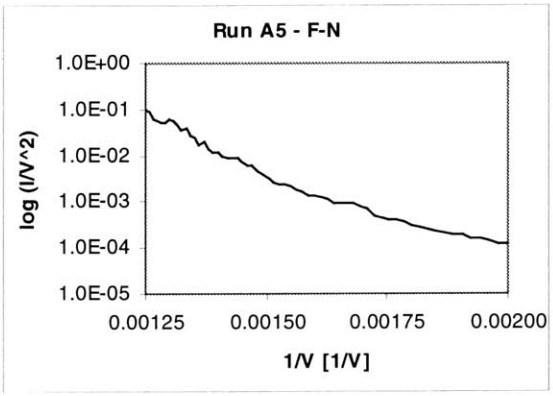
Run A5 - F-N
log (I/V^2)
1.0E+00
1.0E-01
1.0E-02
1.0E-03
1.0E-04
1.0E-05
0.00125
0.00150
0.00175
0.00200
1/V [1/V]

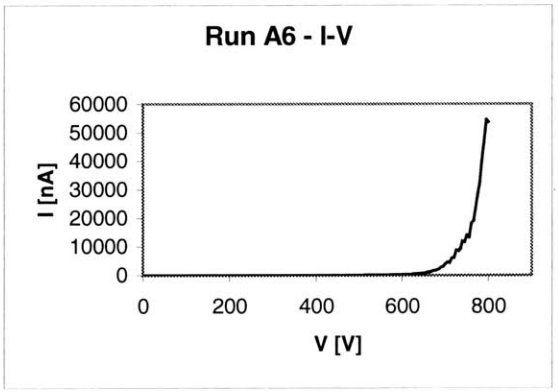
Run A6 - I-V
I [nA]
60000
50000
40000
30000
20000
10000
0
0
200
400
600
800
V [V]

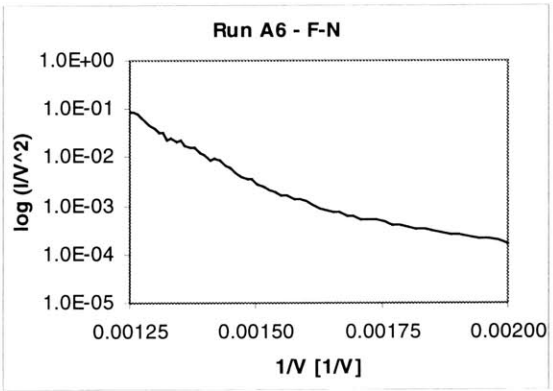
Run A6 - F-N
log (I/V^2)
1.0E+00
1.0E-01
1.0E-02
1.0E-03
1.0E-04
1.0E-05
0.00125
0.00150
0.00175
0.00200
1/V [1/V]

Ti / Pt devices

Run B (200μm^2 contact area)

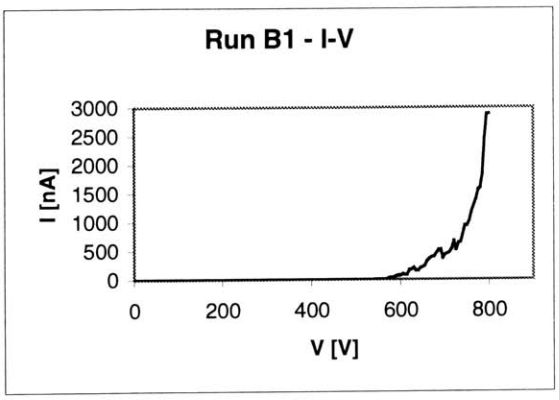

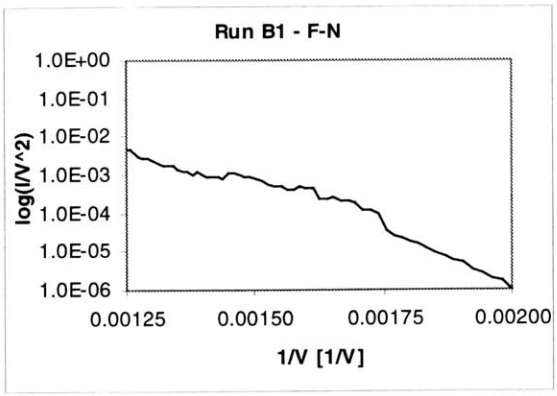

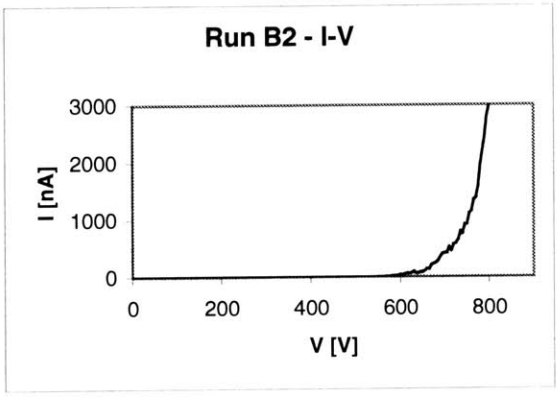

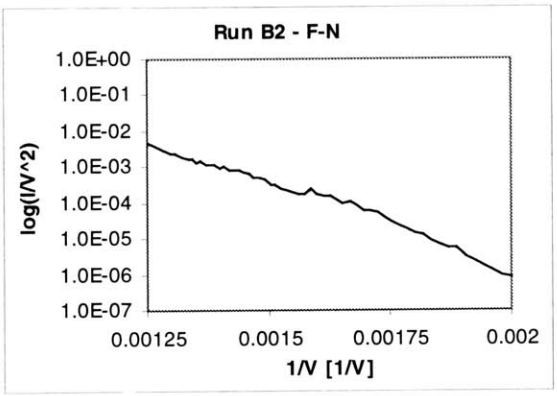

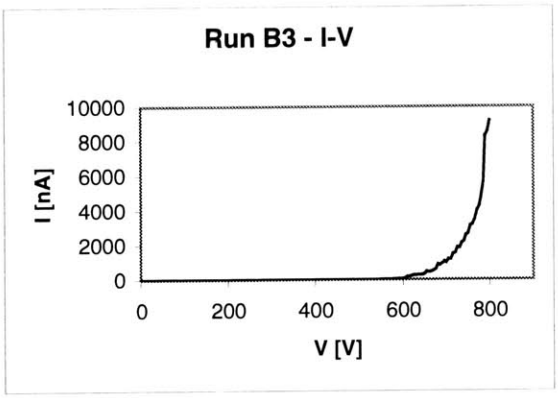

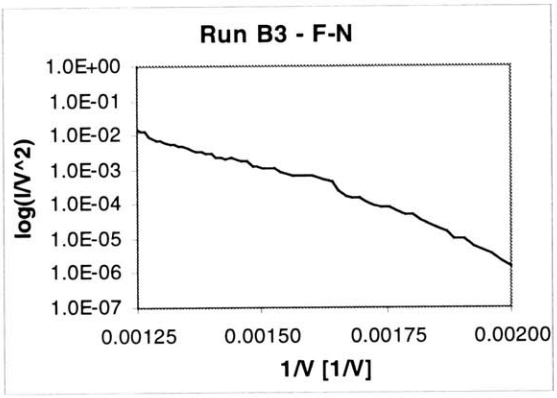

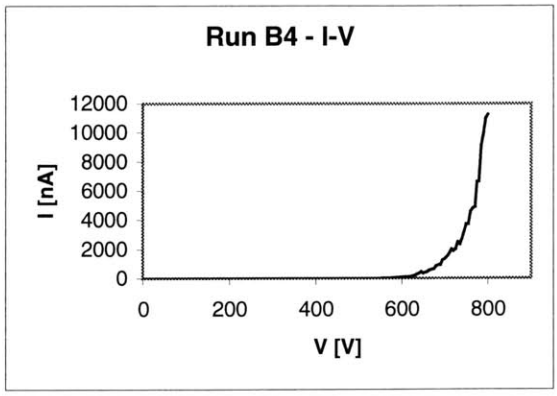
Run B4 - I-V
12000
10000
8000
6000
4000
2000
0
I [nA]
0
200
400
600
800
V [V]

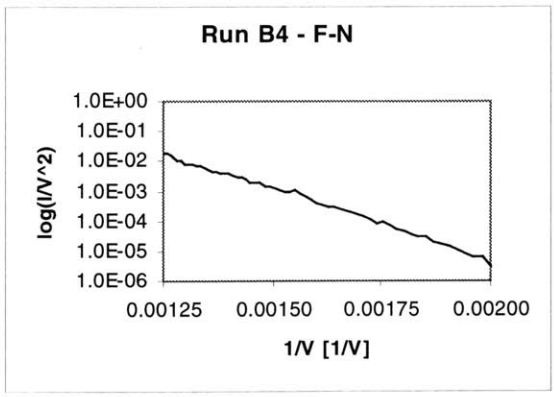
Run B4 - F-N
1.0E+00
1.0E-01
1.0E-02
1.0E-03
1.0E-04
1.0E-05
1.0E-06
log(I/V^2)
0.00125
0.00150
0.00175
0.00200
1/V [1/V]

Ti / Pt devices

Run C (300μm^2 contact area)

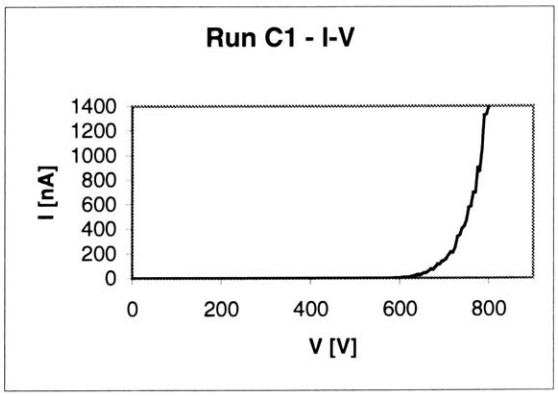

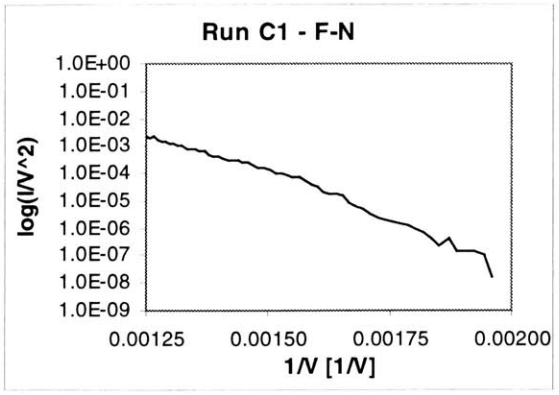

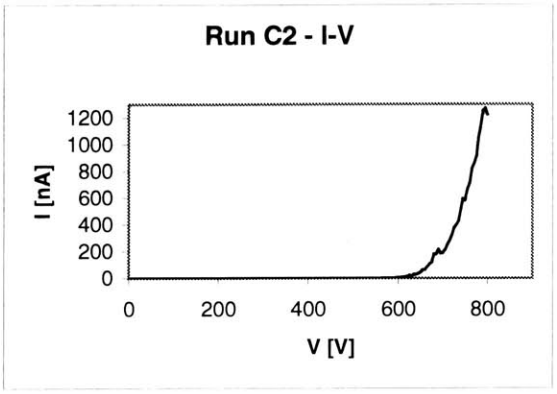

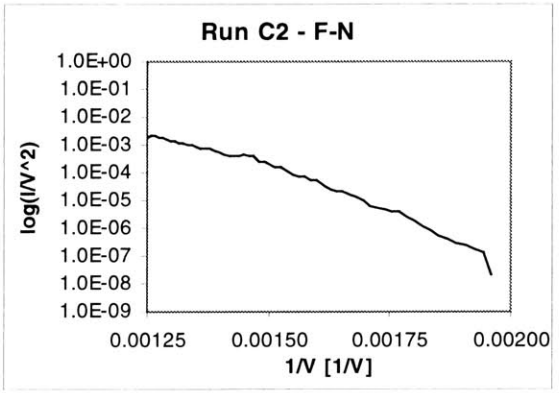

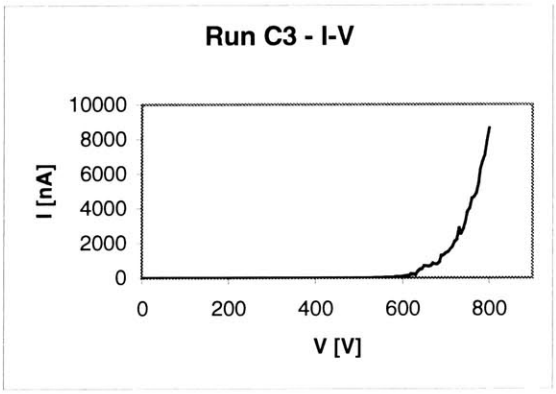

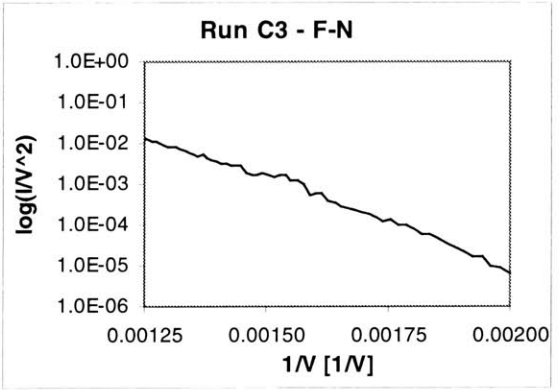

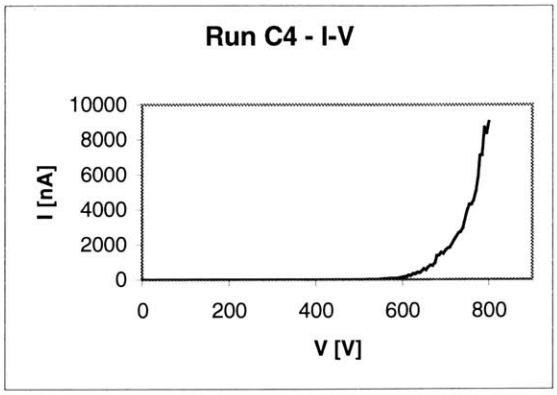
Run C4 - I-V
I [nA]
10000
8000
6000
4000
2000
0
0
200
400
600
800
V [V]

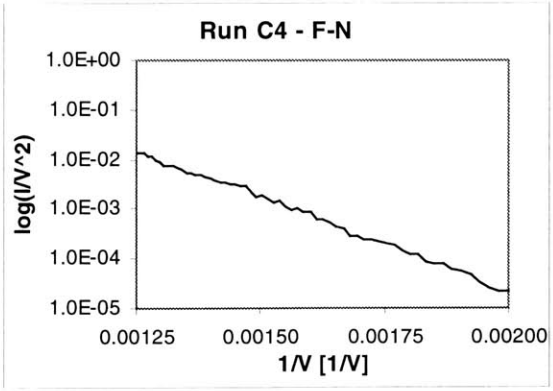
Run C4 - F-N
log(I/V^2)
1.0E+00
1.0E-01
1.0E-02
1.0E-03
1.0E-04
1.0E-05
0.00125
0.00150
0.00175
0.00200
1/V [1/V]

Ti / Ni / NiO (oxidized nickel)

Run G (300μm^2 contact area)

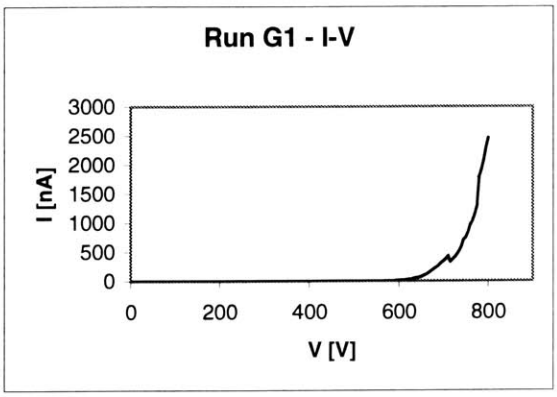

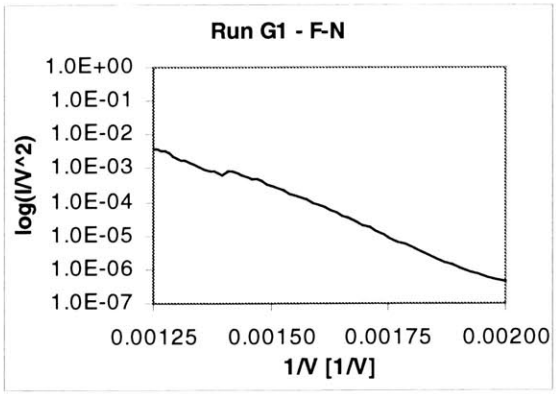

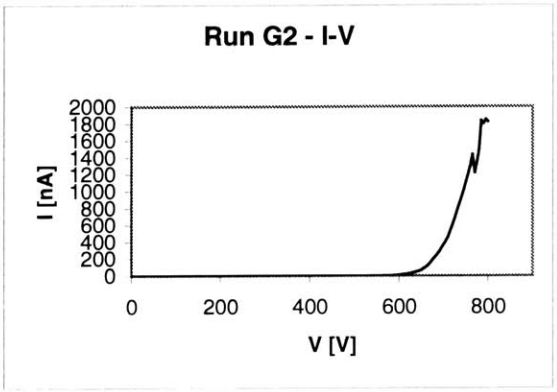

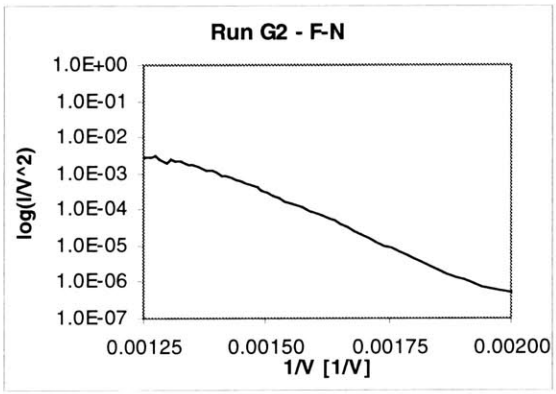

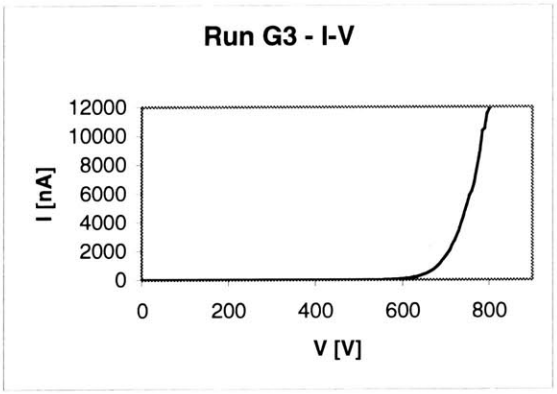

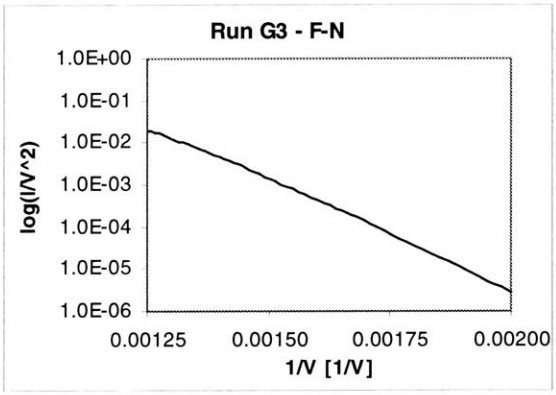

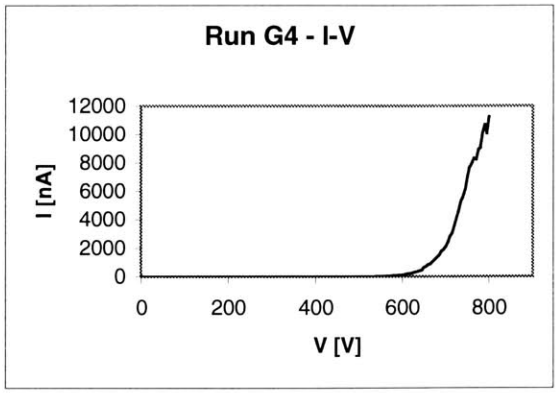
Run G4 - I-V
I [nA]
12000
10000
8000
6000
4000
2000
0
0
200
400
600
800
V [V]

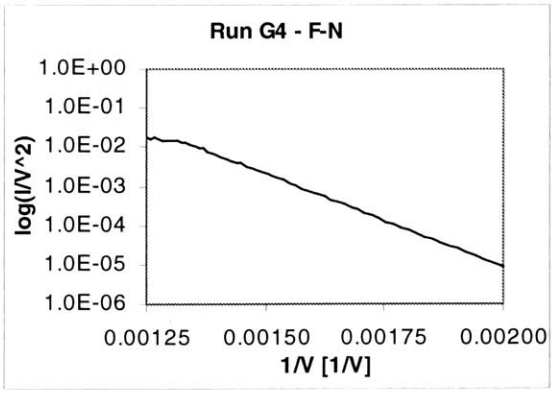
Run G4 - F-N
log(I/V^2)
1.0E+00
1.0E-01
1.0E-02
1.0E-03
1.0E-04
1.0E-05
1.0E-06
0.00125
0.00150
0.00175
0.00200
1/V [1/V]

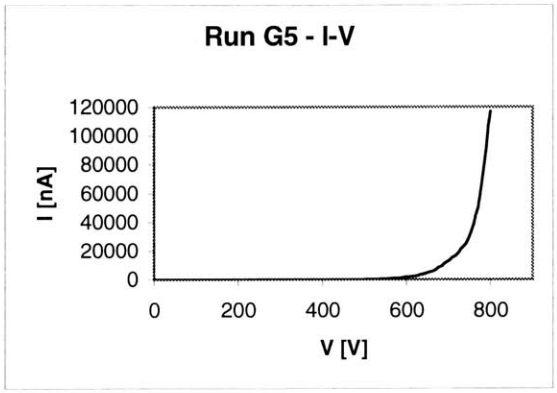
Run G5 - I-V
I [nA]
120000
100000
80000
60000
40000
20000
0
0
200
400
600
800
V [V]

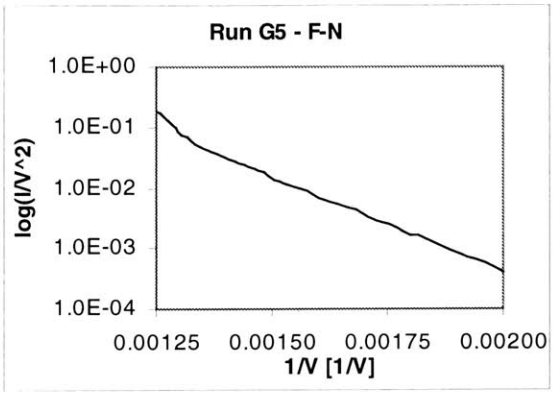
Run G5 - F-N
log(I/V^2)
1.0E+00
1.0E-01
1.0E-02
1.0E-03
1.0E-04
0.00125
0.00150
0.00175
0.00200
1/V [1/V]

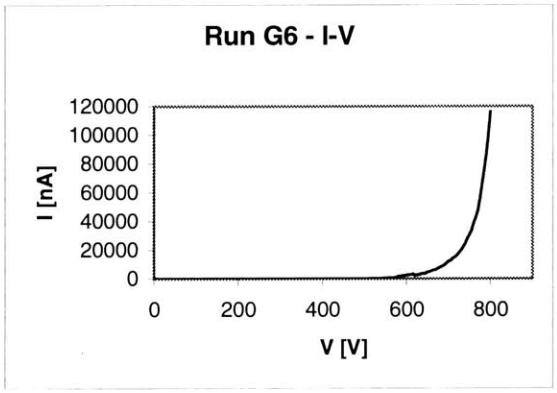
Run G6 - I-V
I [nA]
120000
100000
80000
60000
40000
20000
0
0
200
400
600
800
V [V]

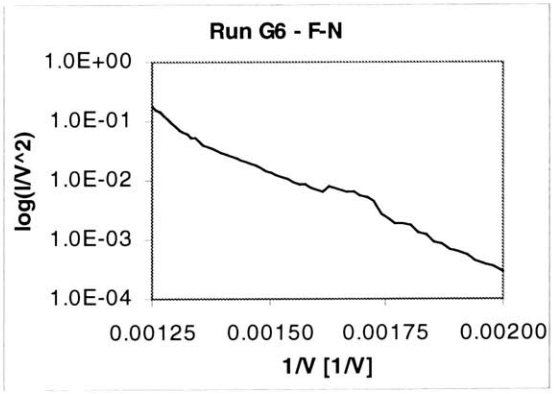
Run G6 - F-N
log(I/V^2)
1.0E+00
1.0E-01
1.0E-02
1.0E-03
1.0E-04
0.00125
0.00150
0.00175
0.00200
1/V [1/V]

Ti / Ni / NiO (oxidized nickel)

Run I (200μm^2 contact area)

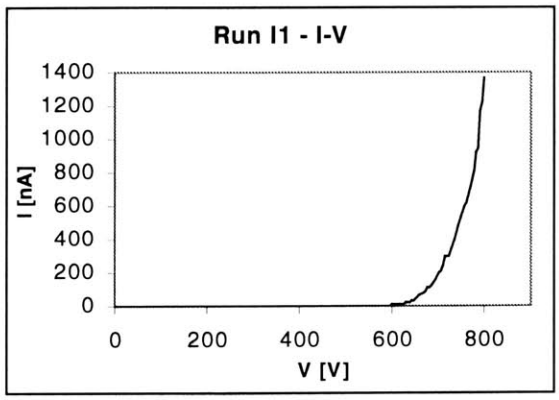

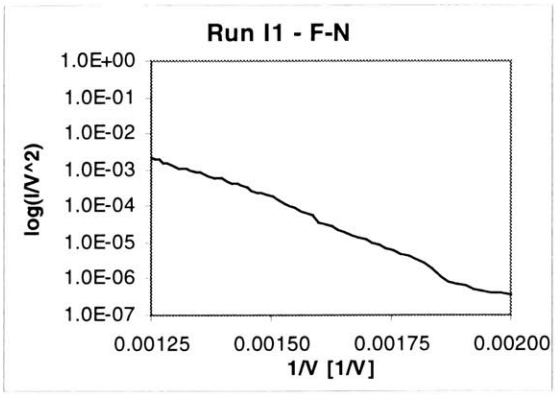

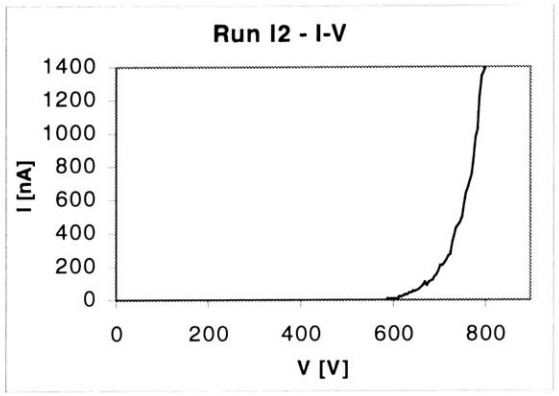

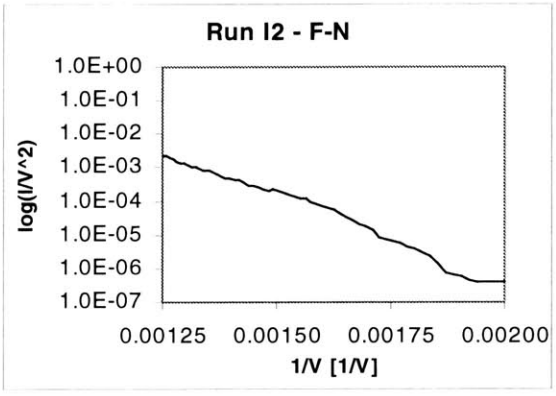

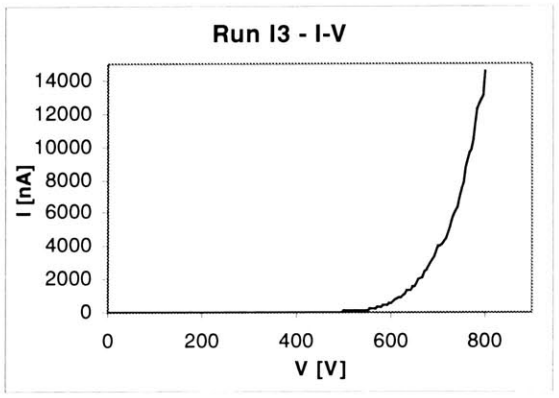

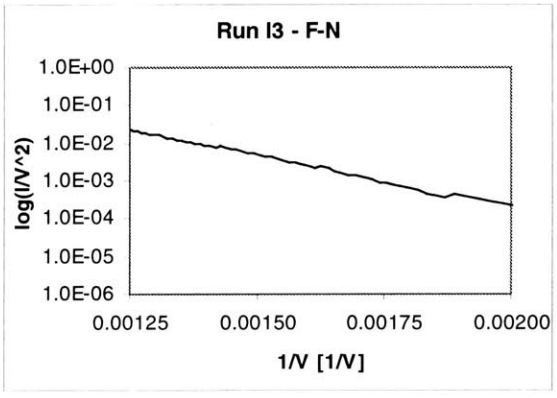

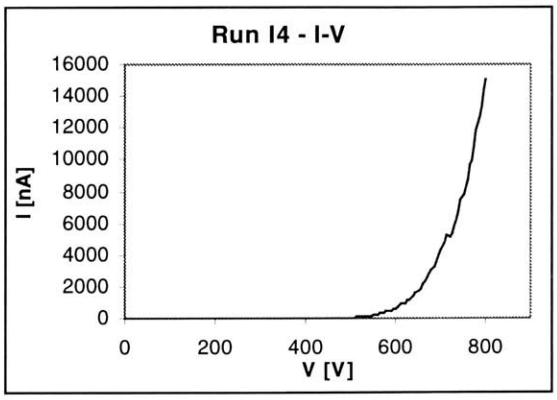
Run I4 - I-V
I [nA]
16000
14000
12000
10000
8000
6000
4000
2000
0
0
200
400
600
800
V [V]

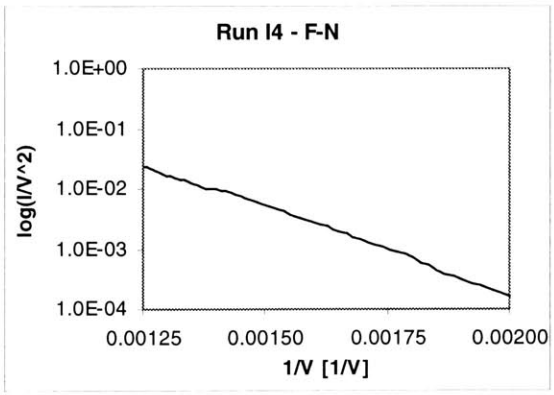
Run I4 - F-N
log(I/V^2)
1.0E+00
1.0E-01
1.0E-02
1.0E-03
1.0E-04
0.00125
0.00150
0.00175
0.00200
1/V [1/V]

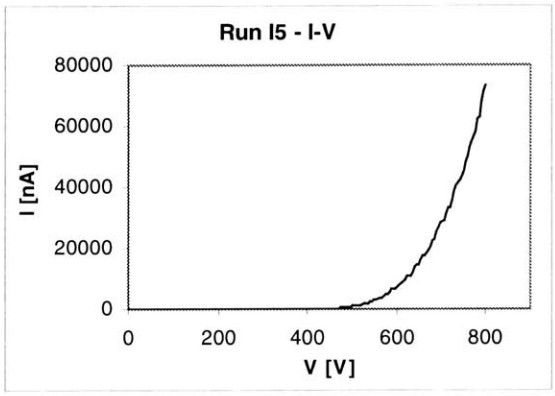
Run I5 - I-V
I [nA]
80000
60000
40000
20000
0
0
200
400
600
800
V [V]

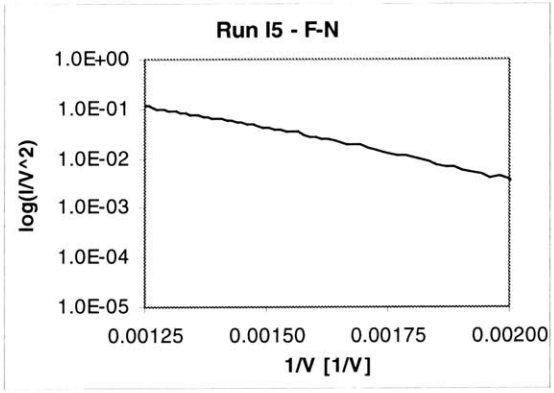
Run I5 - F-N
log(I/V^2)
1.0E+00
1.0E-01
1.0E-02
1.0E-03
1.0E-04
1.0E-05
0.00125
0.00150
0.00175
0.00200
1/V [1/V]

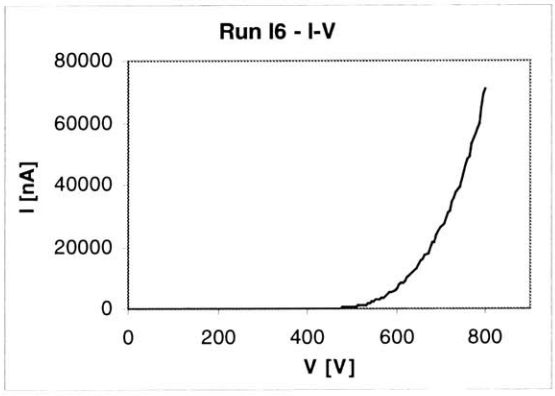
Run I6 - I-V
I [nA]
80000
60000
40000
20000
0
0
200
400
600
800
V [V]

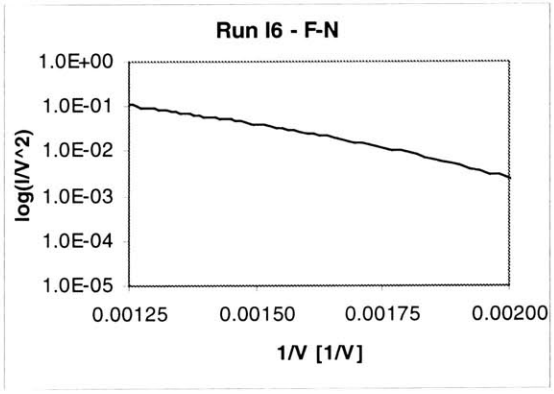
Run I6 - F-N
log(I/V^2)
1.0E+00
1.0E-01
1.0E-02
1.0E-03
1.0E-04
1.0E-05
0.00125
0.00150
0.00175
0.00200
1/V [1/V]

Ti / Ni / NiO (e-beamed nickel oxide)

Run K (100μm^2 contact area)

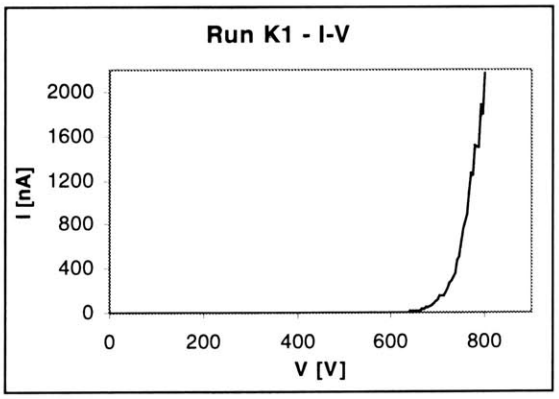

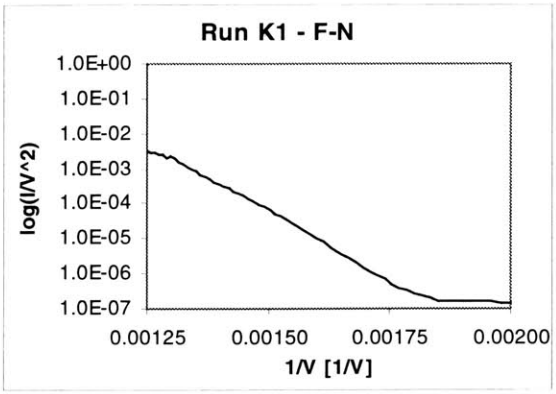

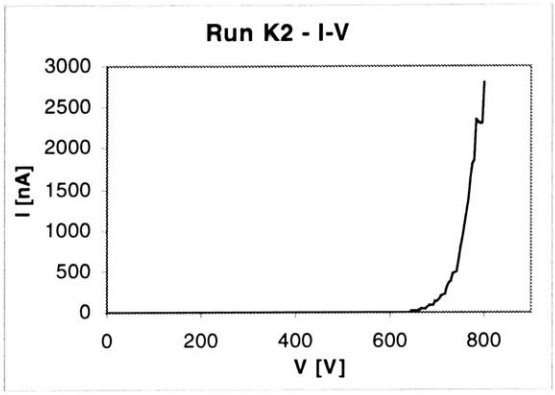

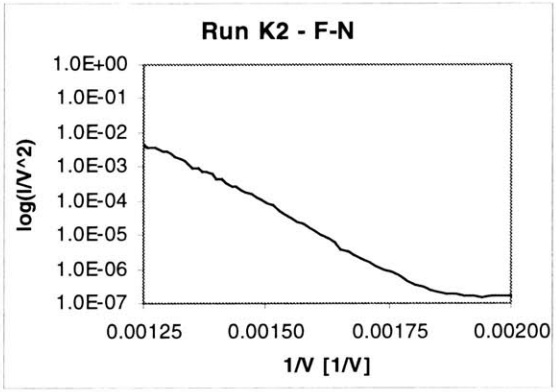

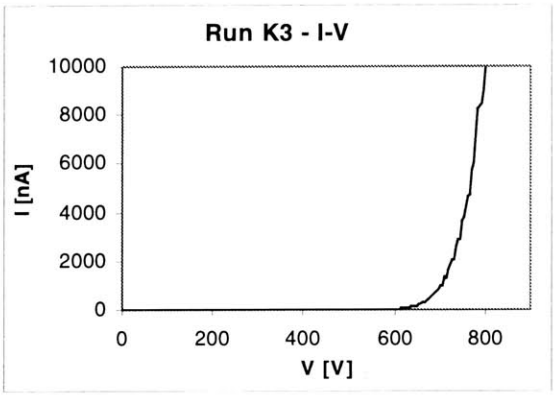

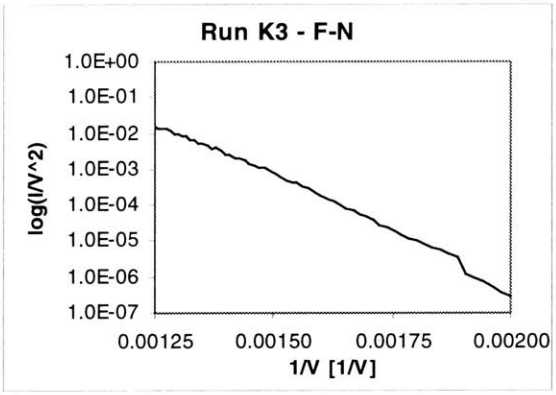

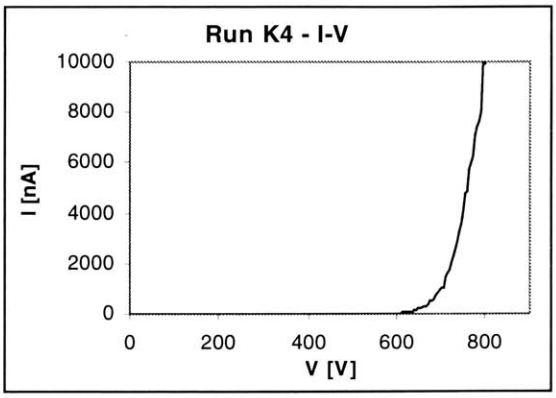
Run K4 - I-V
10000
8000
6000
4000
2000
0
I [nA]
0
200
400
600
800
V [V]

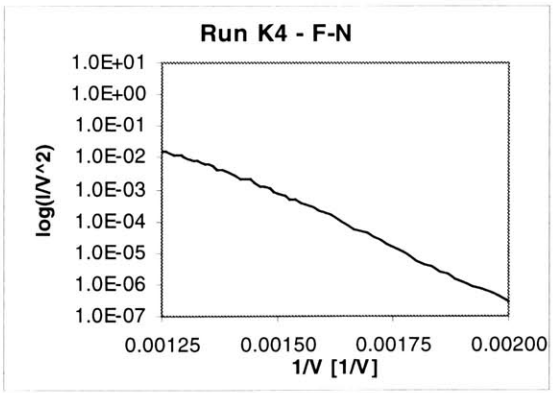
Run K4 - F-N
1.0E+01
1.0E+00
1.0E-01
1.0E-02
1.0E-03
1.0E-04
1.0E-05
1.0E-06
1.0E-07
log(I/V^2)
0.00125
0.00150
0.00175
0.00200
1/V [1/V]

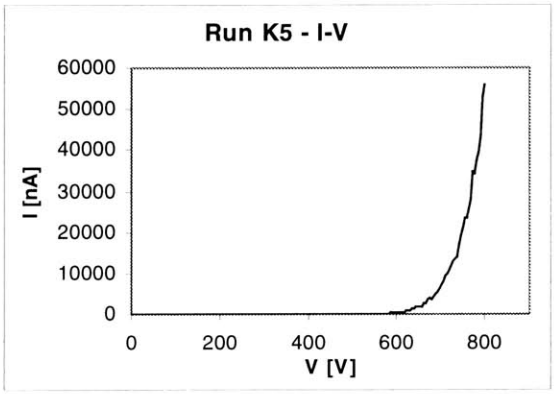
Run K5 - I-V
60000
50000
40000
30000
20000
10000
0
I [nA]
0
200
400
600
800
V [V]

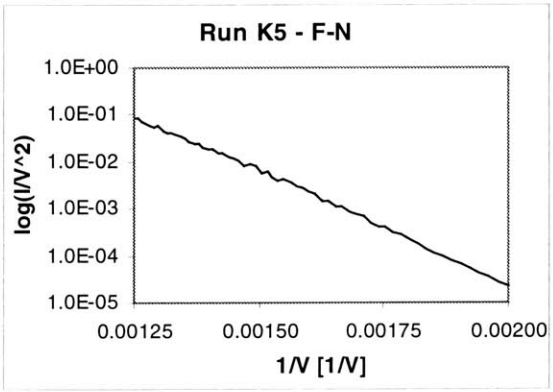
Run K5 - F-N
1.0E+00
1.0E-01
1.0E-02
1.0E-03
1.0E-04
1.0E-05
log(I/V^2)
0.00125
0.00150
0.00175
0.00200
1/V [1/V]

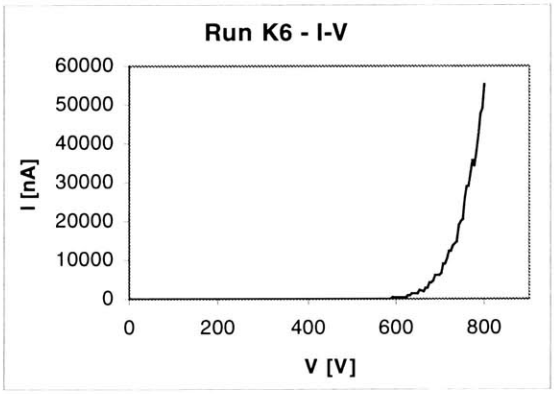
Run K6 - I-V
60000
50000
40000
30000
20000
10000
0
I [nA]
0
200
400
600
800
V [V]

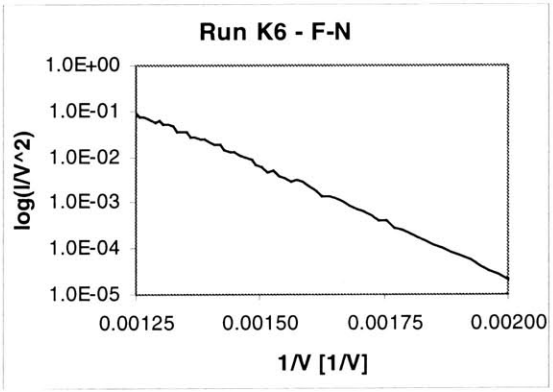
Run K6 - F-N
1.0E+00
1.0E-01
1.0E-02
1.0E-03
1.0E-04
1.0E-05
log(I/V^2)
0.00125
0.00150
0.00175
0.00200
1/V [1/V]

Ti / Ni / NiO (e-beamed nickel oxide)

Run N (30μm^2 contact area)

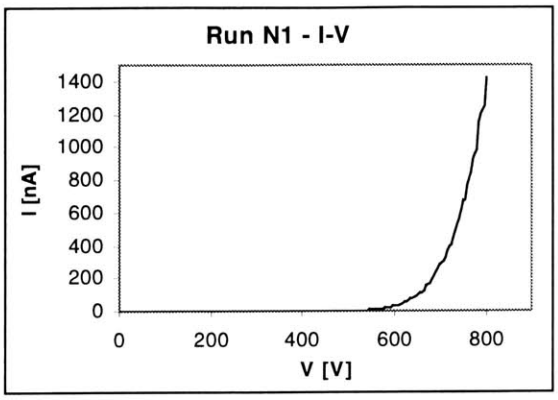

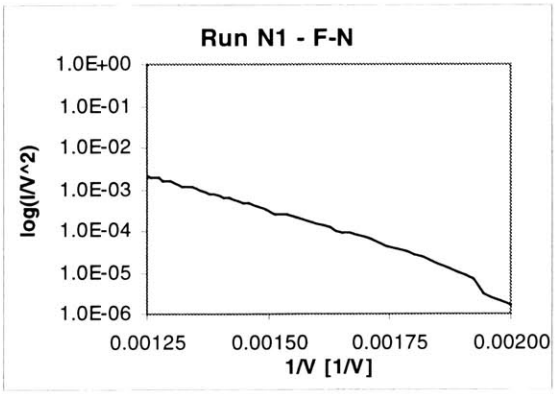

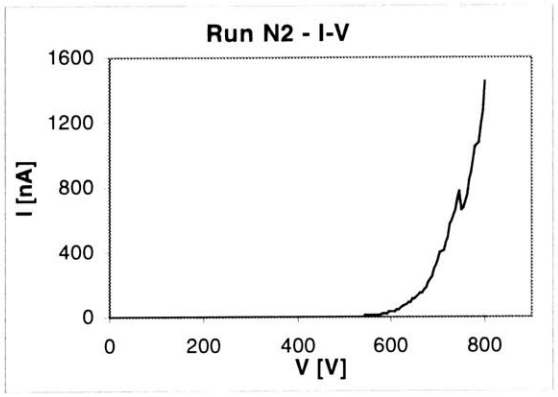

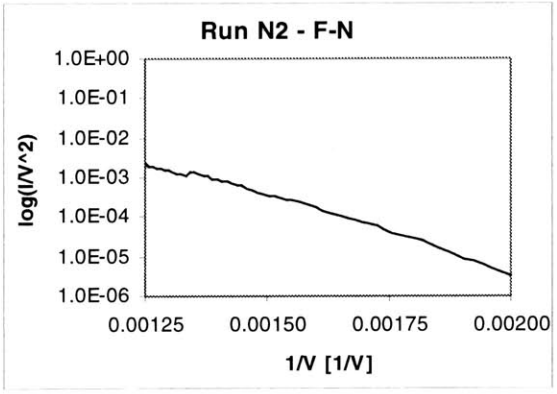

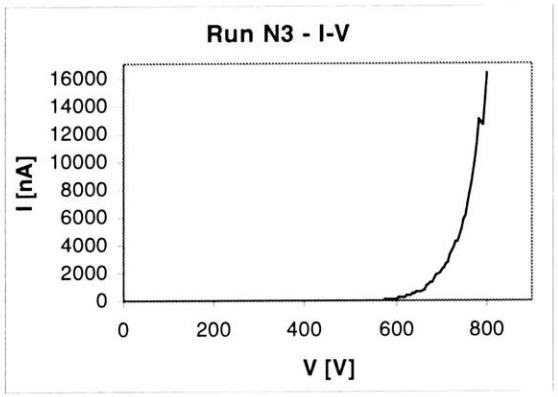

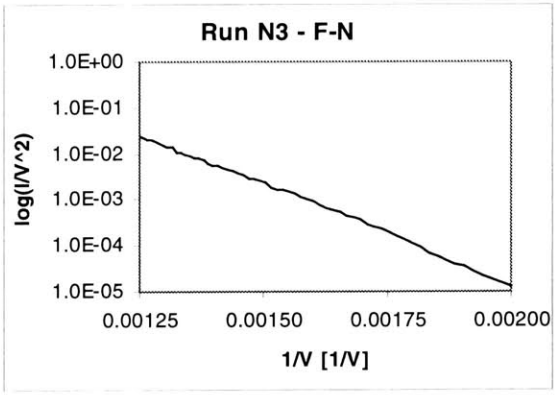

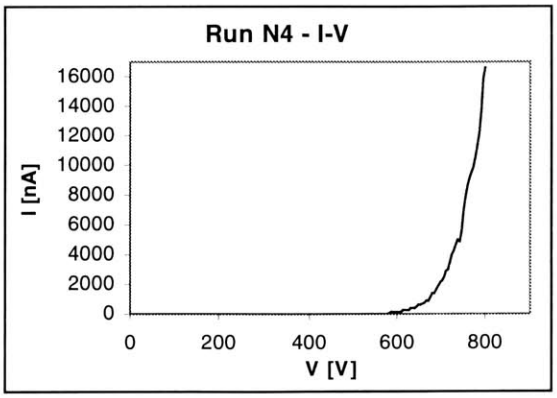
Run N4 - I-V
I [nA]
16000
14000
12000
10000
8000
6000
4000
2000
0
0
200
400
600
800
V [V]

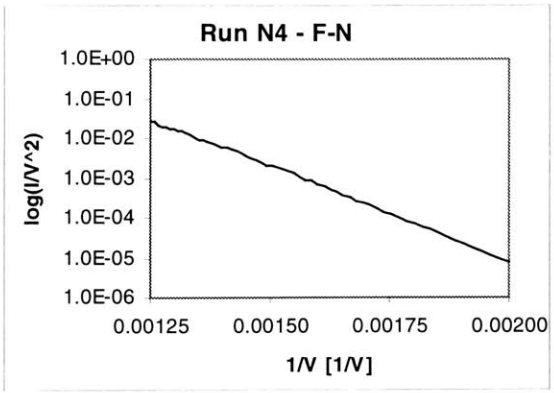
Run N4 - F-N
log(I/V^2)
1.0E+00
1.0E-01
1.0E-02
1.0E-03
1.0E-04
1.0E-05
1.0E-06
0.00125
0.00150
0.00175
0.00200
1/V [1/V]

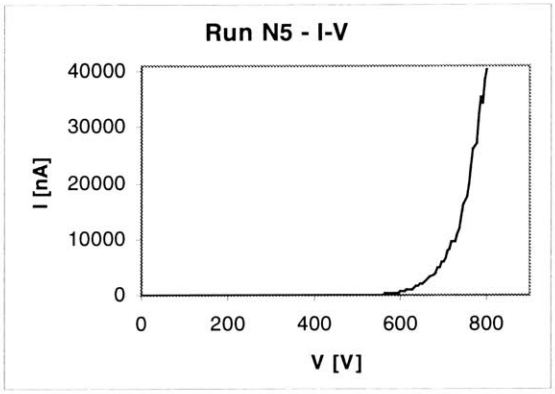
Run N5 - I-V
I [nA]
40000
30000
20000
10000
0
0
200
400
600
800
V [V]

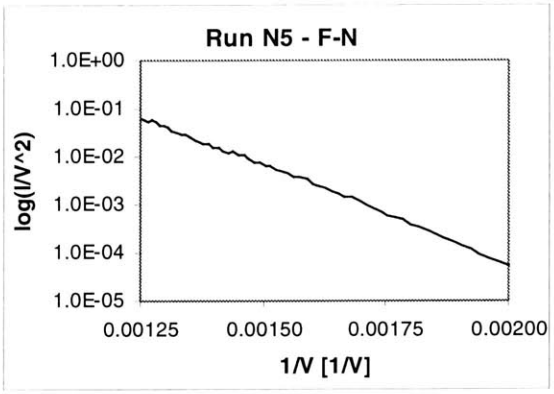
Run N5 - F-N
log(I/V^2)
1.0E+00
1.0E-01
1.0E-02
1.0E-03
1.0E-04
1.0E-05
0.00125
0.00150
0.00175
0.00200
1/V [1/V]

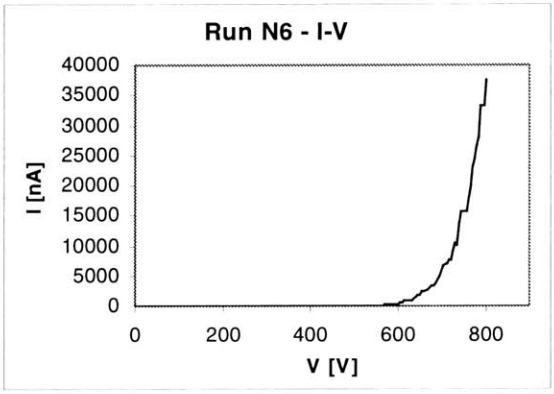
Run N6 - I-V
I [nA]
40000
35000
30000
25000
20000
15000
10000
5000
0
0
200
400
600
800
V [V]

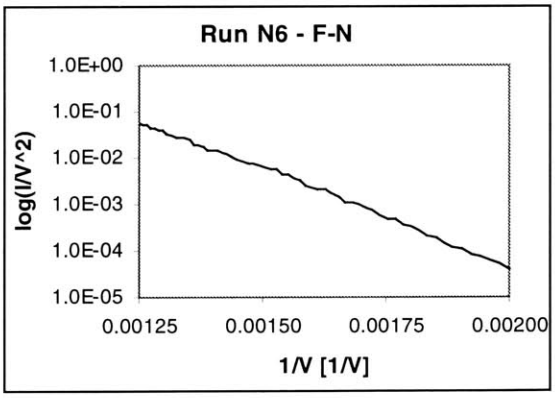
Run N6 - F-N
log(I/V^2)
1.0E+00
1.0E-01
1.0E-02
1.0E-03
1.0E-04
1.0E-05
0.00125
0.00150
0.00175
0.00200
1/V [1/V]

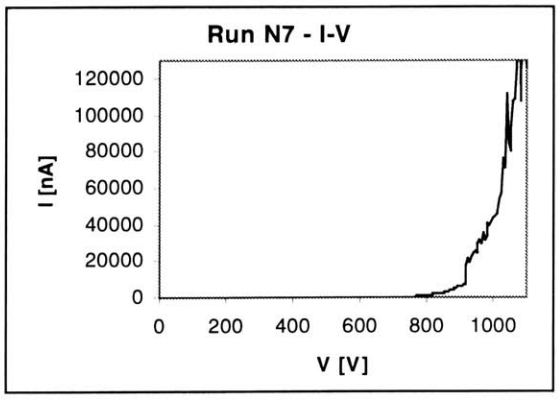
Run N7 - I-V
120000
100000
80000
60000
40000
20000
0
I [nA]
0
200
400
600
800
1000
V [V]

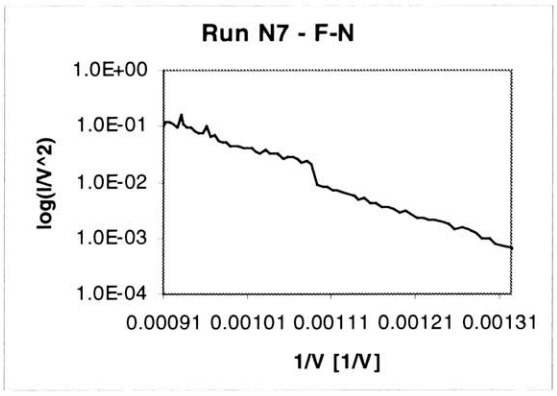
Run N7 - F-N
1.0E+00
1.0E-01
1.0E-02
1.0E-03
1.0E-04
log(I/V^2)
0.00091
0.00101
0.00111
0.00121
0.00131
1/V [1/V]

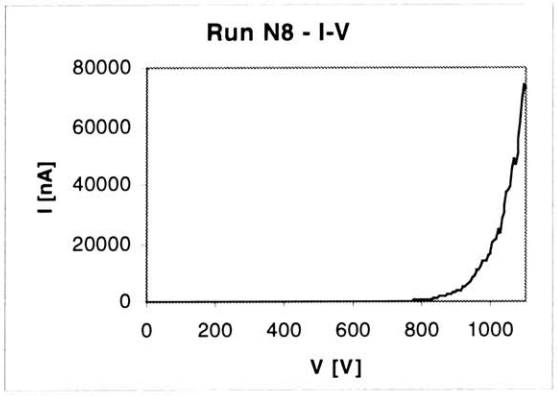
Run N8 - I-V
80000
60000
40000
20000
0
I [nA]
0
200
400
600
800
1000
V [V]

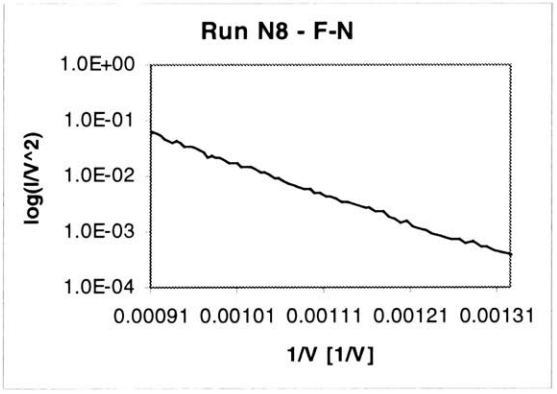
Run N8 - F-N
1.0E+00
1.0E-01
1.0E-02
1.0E-03
1.0E-04
log(I/V^2)
0.00091
0.00101
0.00111
0.00121
0.00131
1/V [1/V]

Bibliography

[1] J. Y. Shim, H. K. Baik, and K. M. Song, "Mechanism of Field Emission from Chemical Vapor Deposited Undoped Polycrystalline Diamond Films," *Journal of Applied Physics 87*, 10, 2000, p. 7508-18.

[2] M. W. Geis, J. C. Twichell, C. O. Bozler, D. D. Rathman, N. N. Efremow, K. E. Krohn, M. A. Hollis, R. Uttaro, T. M. Lyszczarz, and M. Kordesch, "Diamond Field-Emission Cathodes," *Sixth International IEEE Microelectronics Conference Technical Digest*, 1993, p. 160-1.

[3] J. van der Weide, Z. Zhang, P. K. Baumann, M. G. Wensell, J. Bernholc, and R. J. Nemanich, "Negative Electron Affinity Effects on the Diamond (100) Surface," *Physical Review B 50*, 8, 1994, p. 5803-6.

[4] W. Zhu, G. P. Kochanski, S. Jin, and L. Seibles, "Defect-enhanced Electron Field Emission from Chemical Vapor Deposited Diamond," *Journal of Applied Physics 78*, 4, 1995, p. 2707-11.

[5] P. Lerner, P. H. Cutler, and N. M. Miskovsky, "Theoretical Analysis of Field Emission from a Metal Diamond Cold Cathode Emitter," *Journal of Vacuum Science and Technology B 15*, 2, 1997, p. 337-42.

[6] O. Gröning, O. M. Küttel, P. Gröning, and L. Schlapbach, "Field Emitted Electron Energy Distribution from Nitrogen-Containing Diamondlike Carbon," *Applied Physics Letters 71*, 16, 1997, p. 2253-5.

[7] C. Bandis and B. B. Pate, "Simultaneous Field Emission and Photoemission from Diamond," *Applied Physics Letters 69*, 3, 1996, p. 366-8.

[8] J.-M. Bonard, F. Maier, T. Stockli, A. Chatelain, W. A. deHeer, J.-P. Salvetat, and L. Forro, "Field Emission Properties of Multi-walled Carbon Nanotubes," *Ultramicroscopy 73*, 1-4, 1998, p. 7-15.

[9] S. Uemura, T. Nagasako, J. Yotani, and T. Shimojo, "Carbon Nanotube FED Elements," *Society for Information Display Symposium Digest 1998*, p. 1052-105.

[10] N. W. Ashcroft and N. D. Mermin, *Solid-State Physics*, Harcourt Brace College Publishers, New York, 1976.

[11] R. Gomer, *Field Emission and Field Ionization*, American Institute of Physics, New York, 1993.

[12] D. G. Pflug, *Modeling the Effects of Device Scaling on Field Emitter Array Performance*, Massachusetts Institute of Technology, Cambridge, 1996.

[13] Y. Saito, K. Hamaguchi, K. Hata, K. Tohji, A. Kasuya, Y. Nishina, K. Uchida, Y. Tasaka, F. Ikazaki, and M. Yumura, "Field Emission from Carbon Nanotubes: Purified Single-Walled and Multi-Walled Tubes," *Ultramicroscopy 73*, 1-4, 1998, p. 1-6.

[14] S. Bandow, S. Asaka, X. Zhao, and Y. Ando, "Purification and Magnetic Properties of Carbon Nanotubes," *Applied Physics A 67*, 1, 1998, p. 23-27.

[15] C. Journet and P. Bernier, "Production of Carbon Nanotubes," *Applied Physics A 67*, 1, 1998, p. 1-9.

[16] R. Saito, G. Dresselhaus, and M. S. Dresselhaus, *Physical Properties of Carbon Nanotubes*, Imperial College Press, London, 1998.

[17] P. Avouris, T. Hertel, R. Martel, T. Schmidt, H. R. Shea, and R. E. Walkup, "Carbon Nanotubes: Nanomechanics, Manipulations, and Electronic Devices," *Applied Surface Science 141*, 3-4, 1999, p. 201-9.

[18] A. DeVita, J.-C. Charlier, X. Blase, and R. Car, "Electronic Structures at Carbon Nanotube Tips," *Applied Physics A 68*, 3, 1999, p. 283-6.

[19] G. S. Duesberg, J. Muster, H. J. Byrne, S. Roth, and M. Burghard, "Towards Processing of Carbon Nanotubes for Technical Applications," *Applied Physics A 69*, 3,1999, p. 269-74.

[20] T. Hertel, R. Martel, and P. Avouris, "Manipulation of Individual Carbon Nanotubes and Their Interaction with Surfaces," *Journal of Physical Chemistry B 102*, 6, 1993, p. 910-5.

[21] R. Saito, G. Dresselhaus, and M. S. Dresselhaus, "Tunneling Conductance of Connected Carbon Nanotubes," *Physical Review B – Condensed Matter 53*, 4, 1996, pp. 2044-50.

[22] A. Hassanien, M. Tokumoto, Y. Kumazawa, H. Kataura, Y. Maniwa, S. Suzuki, and Y. Achiba, "Atomic Structure and Electronic Properties of Single-Wall Carbon Nanotubes Probed by Scanning Tunneling Microscope at Room Temperature," *Applied Physics Letters 73*, 26, 1998, p. 3839-41.

[23] J. Nygård, D.H. Cobden, M. Bockrath, P. L. McEuen, and P.E. Lindelof, "Electrical Transport Measurements on Single-Walled Carbon Nanotubes," *Applied Physics A, vol. 69*, 3, 1999, p. 297-304.

[24] A. Thess, R. Lee, P. Nikolaev, H. Dai, P. Petit, J. Robert, C. Xu, Y. H. Lee, S. G. Kim, A. G. Rinzler, D. T. Colbert, G. Scuseria, D. Tománek, J. E. Fischer, and R. E. Smalley, "Crystalline Ropes of Metallic Carbon Nanotubes," *Science 273*, 5274, 1996, p. 483-7.

[25] H. Ago, T. Kugler, F. Cacialli, W. R. Salaneck, M. S. P. Shaffer, A. H. Windle, and R. H. Friend, "Work Functions and Surface Functional Groups of Multiwall Carbon Nanotubes," *Journal of Physical Chemistry B, vol. 103*, 38, 1999, p. 8116-21.

[26] A. N. Obraztsov, A.P. Volkov, I.Y. Pavlovskii, A. L. Chuvilin, N.A. Rudina, and Kuznetsov, "Role of the Curvature of Atomic Layers in Electron Field Emission from Graphitic Nanostructured Carbon," *JETP Letters 69*, 5, 1999, p. 411-7.

[27] W.A. deHeer, J.-M. Bonard, T. Stockli, A. Chatelain, L. Forro, and D. Ugarte, "Carbon Nanotube Films: Electronic Properties and Their Application as Field Emitters," *Zeitschrift fur Physik D – Atoms, Molecules, and Clusters, 40*, 1-4, 1997, p. 418-20.

[28] W. B. Choi, D. S. Chung, S. H. Park, J. M. Kim, "A 4.5-Inch Fully Sealed Carbon Nanotube-Based Field Emission Flat Panel Display," *Society for Information Display Digest 1999*, p. 1134-7.

[29] W.C. Yeh and M. Matsumura, "Chemical Vapor Deposition of Nickel Oxide Films from Bis-π-Cyclopentadienyl-Nickel," *Japanese Journal of Applied Physics 36 part 1*, 11, 1997, p. 6884-7.

[30] J. C. de Jesús, P. Pereira, J. Carrazza, and F. Zaera, "Influence of Argon Ion Bombardment on the Oxidation of Nickel Surfaces," *Surface Science 369*, 1-3, 1996, p. 217-30.

[31] N. Birks and G. H. Meier, *Introduction to High Temperature Oxidation of Metals*, Edward Arnold Publishers Ltd, London, 1983.

[32] F. P. Fehlner, *Low-Temperature Oxidation*, John Wiley & Sons, New York, 1986.

[33] S. Mitra, S. R. Tatti, and J. P. Stark, "A Spectroscopic Study of Nickel Oxide Films on Polycrystalline Nickel," *Thin Solid Films 177*, 1989, p 171-80.

[34] G. Wakefield, P. J. Dobson, Y. Y. Foo, A. Loni, A. Simons, and J. L. Hutchison, "The Fabrication and Characterization of Nickel Oxide Films and Their Application as Contacts to Polymer/Porous Silicon Electroluminescent Devices," *Semiconductor Science Technology 12*, 10, 1997, p. 1304-9.

[35] D. R. Lide ed., *CRC Handbook of Chemistry and Physics 75th ed.*, CRC Press, Ann Arbor, 1994.

[36] Rice University, Tubes@Rice, http://cnst.rice.edu/tubes/production.html, 1999.

[37] A. G. Rinzler, J. Liu, H. Dai, .P. Nikolaev, C. B. Huffman, F. J. Rodríguez-Macías, P. J. Boul, A. H. Lu, D. Heymann, D. T. Colbert, R. S. Lee, J. E. Fischer, A.

M. Rao, P. C. Eklund, and R. E. Smalley, "Large-Scale Purification of Single-Wall Carbon Nanotubes: Process, Product, and Characterization," *Applied Physics A. 67*, 1, 1998, p. 29-37.

[38] P. Lerner, N. M. Miskovsky, and P. H. Cutler, "Model Calculations of Internal Field Emission and J-V Characteristics of a Composite n-Si and N-Diamond Cold Cathode Source," *Journal of Vacuum Science and Technology B 16*, 2, 1998, p. 900-5.

[39] A. T. Fromhold, Jr., *Quantum Mechanics for Applied Physics and Engineering*, Academic Press, New York, 1981.

[40] S. Gasiorowicz, *Quantum Physics*, John Wiley and Sons Inc., New York, 1974.

[41] T. Kado and T. Yamada, "Preparation and Structural Analysis of Nickel/Nickel Oxide Multilayers," *Journal of Applied Physics 77*, 12, 1995, 6651-7.

[42] E. Fujii, A. Tomozawa, H. Torii, R. Takayama, "Preferred Orientations of NiO Films Prepared by Plasma-Enhanced Metalorganic Chemical Vapor Deposition," *Japanese Journal of Applied Physics 35 part 2*, 3A, 1996, p. L328-30.

[43] S. Mitra, "Investigation of Diffusion Mechanisms During Nickel Oxide Film Growth by an Isotope Separation Technique," *Materials Science and Engineering A174*, 1, 1994, p. 103-10.

[44] J. Feinleib and D. Adler, "Band Structure and Electrical Conductivity of NiO," *Physical Review Letters 21*, 14, 1968, p 1010-3.

238 - 39